



FORTH/IESL

ΕΘΚΤΗ/ΙΕΣΤ



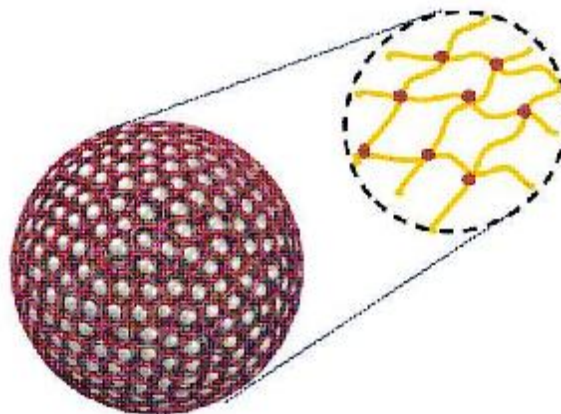
University of Crete  
**Material Science and  
Technology Department**

Foundation for Research and Technology  
**Institute of Electronic Structure and Lasers**



*Master Thesis:*

“Synthesis and characterization of porous  
polymer nanoparticles for gas separation  
applications”



*Charikleia Flouraki*

*Supervisor: Prof. Maria Vamvakaki*

Heraklion, 2014

## Ευχαριστίες

Η παρούσα μεταπτυχιακή εργασία δεν θα μπορούσε να ολοκληρωθεί χωρίς την πολύτιμη βοήθεια και υποστήριξη ορισμένων ανθρώπων τους οποίους θα ήθελα να ευχαριστήσω θερμά.

Πρώτα από όλους, ευχαριστώ την επιβλέπουσα καθηγήτρια μου κ. Μαρία Βαμβακάκη για την δυνατότητα που μου έδωσε να πραγματοποιήσω την μεταπτυχιακή μου εργασία στον τομέα της σύνθεσης πολυμερών. Με στήριξε και με βοήθησε με τις συμβουλές της αλλά με μάλωνε κιόλας όταν δεν φορούσα τα γυαλιά μου. Επιπλέον ευχαριστώ θερμά την Δρ. Μαρία Καλύβα για την καθοδήγηση, τις συμβουλές και την βοήθεια που μου πρόσφερε κατά την διεξαγωγή των πειραμάτων καθώς και στην αξιολόγηση των αποτελεσμάτων. Με έμαθε να μπορώ να στέκομαι μόνη μου στο εργαστήριο και αυτό είναι πολύ σημαντικό για μένα.

Επιπλέον οφείλω ένα μεγάλο ευχαριστώ στον καθηγητή κ. Γεράσιμο Αρματά για την βοήθεια του στην υλοποίηση, στην ανάλυση και αξιολόγηση των πειραμάτων προσρόφησης καθώς και για την συμμετοχή του στην τριμελή μου επιτροπή. Σε αυτό το σημείο θα ήθελα να ευχαριστήσω και τον Δρ. Ιωάννη Παπαδά για όλες τις μετρήσεις προσρόφησης καθώς και για τις μετρήσεις επιφάνειας των δειγμάτων μου καθώς χωρίς την βοήθεια του δεν θα είχε ολοκληρωθεί η παρούσα εργασία.

Ευχαριστώ επίσης τον καθηγητή κ. Γεώργιο Πετεκίδη για την τιμή που μου έκανε να συμμετέχει στην τριμελή μου επιτροπή.

Ευχαριστώ όλο το υπόλοιπο group, παλιά και νέα μέλη, για το ευχάριστο κλίμα εντός του εργαστηρίου και για την βοήθεια τους που είτε την ζητούσα είτε όχι την πρόσφεραν απλόχερα. Ευχαριστώ παιδιά!!

Τέλος , ευχαριστώ πάρα πολύ την οικογένεια μου και ειδικότερα την μητέρα μου χωρίς την υποστήριξη της οποίας δεν θα βρισκόμουν εδώ σήμερα. Εύχομαι να τους έχω κάνει περήφανους.

## **Table of Contents**

Abstract.....	1
<b>1 Introduction.....</b>	<b>2</b>
1.1 Porous materials.....	2
1.2 Porous polymers.....	3
1.3 Porphyrins and metalloporphyrins.....	4
1.3.1 Porphyrin-containing polymers.....	5
1.4 Gas sorption.....	6
1.4.1 Porous materials for gas sorption.....	8
1.4.2 Types of adsorption isotherms.....	8
1.4.3 Gas adsorption theory.....	10
1.4.4 DFT method for pore size distribution.....	11
1.4.5 Ideal Adsorbed Solution Theory (IAST).....	13
1.5 Emulsion polymerization.....	14
1.5.1 Emulsion polymerization intervals.....	17
1.6 Current study.....	19
1.7 References.....	21
<b>2 Experimental .....</b>	<b>23</b>
2.1 Experimental process.....	23
2.1.1 Materials.....	23
2.1.2 Polystyrene particles.....	25

2.1.3	Porphyrin functionalization reaction.....	25
2.1.4	Synthesis of porphyrin-containing particles.....	26
2.2	Sample preparation .....	26
2.2.1	Scanning Electron Microscopy (SEM) .....	26
2.2.2	Transmission Electron Microscopy (TEM).....	27
2.2.3	Dynamic Light Scattering (DLS).....	27
2.2.4	Ultraviolet/visible Spectroscopy (UV/Vis).....	27
2.2.5	Nuclear Magnetic Resonance (NMR).....	27
2.2.6	Supercritical Point Drying (SPD).....	27
2.2.7	Gas adsorption Isotherms.....	28
<b>3</b>	<b>Results and Discussion .....</b>	<b>29</b>
3.1	Synthesis of cross-linked polystyrene nanoparticles .....	29
3.1.1	Polystyrene nanoparticles using different percentage of AOT.....	29
3.2	Highly cross-linked polystyrene particles.....	31
3.2.1	Highly cross-linked polystyrene nanoparticles using different percentage of AOT .....	32
3.3	Porphyrin functionalization reaction.....	35
3.4	Porphyrin containing highly cross-linked polystyrene nanoparticles.....	36
3.4.1	Porphyrin containing particles with 1 wt % AOT.....	36
3.4.2	Porphyrin containing particles with 5 wt % AOT .....	38
3.4.3	Porphyrin content of the particles with 5 wt % AOT.....	42

3.4.3.1 Calibration curve of porphyrin solutions.....	42
3.4.3.2 UV/Vis characterization of the porphyrin containing colloidal particles.....	44
3.4.4 Drying of the samples with supercritical point drying.....	46
3.4.5 Surface area measurements of the porphyrin containing particles.....	48
3.4.5.1 Adsorption/desorption isotherms.....	49
3.4.6 Selectivity of CO <sub>2</sub> over CH <sub>4</sub> .....	53
3.5 References.....	55
<b>4 Conclusions.....</b>	<b>56</b>
<b>5 Characterization Techniques.....</b>	<b>59</b>
5.1 Scanning Electron Microscopy (SEM).....	59
5.2 Transmission Electron Microscopy (TEM).....	60
5.3 Dynamic light scattering (DLS).....	62
5.4 Ultraviolet/visible spectroscopy (UV/Vis).....	64
5.5 <sup>1</sup> H NMR spectroscopy.....	65

## **Abbreviations**

<b>AOT</b>	Dioctyl sulfosuccinate, sodium salt
<b>DLS</b>	dynamic light scattering
<b>DMF</b>	N,N-dimethylformamide
<b>DVB</b>	divinylbenzene
<b>EtOH</b>	ethanol
<b>HCl</b>	hydrochloric acid
<b>MCl</b>	methacryloyl chloride
<b>NMR</b>	nuclear magnetic resonance
<b>PO-S-D</b>	porphyrin-styrene-divinylbenzene
<b>PS</b>	polystyrene
<b>R<sub>h</sub></b>	hydrodynamic radius
<b>SEM</b>	scanning electron microscopy
<b>SPD</b>	Supercritical point drying
<b>St</b>	styrene
<b>TEA</b>	Triethylamine
<b>TEM</b>	transmission electron microscopy
<b>THF</b>	tetrahydrofuran
<b>UV/Vis</b>	Ultraviolet/visible spectroscopy

## **Abstract**

In the past decades, environmental issues have attracted a lot of research attention due to climate changes, global warming and limitations of the energy resources. The rising levels of CO<sub>2</sub> emissions causing global warming demand the development of novel processes based on advanced materials for CO<sub>2</sub> capture. Moreover, a promising solution both environmentally and economically for the energy power problem is biogas which consists mainly of methane (CH<sub>4</sub> ~55-80 vol %) and CO<sub>2</sub> (~20-45 vol %). However, to be effective as a fuel, biogas has first to be purified from its substantial amount of CO<sub>2</sub> and the lower fraction of H<sub>2</sub>S (~0-1 vol %), since these gases reduce its energy content and also lead to the corrosion of the natural gas pipelines. Microporous organic polymers with certain properties including large surface areas, narrow pore size distribution, and high chemical and thermal stability are excellent candidates for potential applications in gas capture and separation. In response to that, we report a simple and facile method for the synthesis of porous porphyrin containing polystyrene particles.

The synthesis is based on the development of a tetra-methacrylate functionalized porphyrin derivative via an esterification reaction of a tetrahydroxy porphyrin analogue which served as a tetra-functional cross-linker. The porous cross-linked polymer nanoparticles were synthesized by free-radical emulsion copolymerization of styrene (St) with the tetra-methacrylate functionalized monomer 5,10,15,20-Tetrakis(4-hydroxyphenyl)-21H,23H-porphine (PO) and the bifunctional cross-linker divinylbenzene (DVB). The cross-link density of the polymer network was varied by keeping the St/cross-linker mole ratio constant at 40/60 and progressively increasing the PO mole ratio from 0.9 to 12 mole % with respect to the total monomer and cross-linker content. The morphology and the size of the nanoparticles were characterized by scanning electron microscopy (SEM), transmission electron microscopy (TEM) and dynamic light scattering (DLS) measurements. The experimental fraction of the porphyrin moieties incorporated within the particles was determined by UV/Vis measurements. The permanent porosity of the PO-S-D materials was confirmed by nitrogen and carbon dioxide adsorption experiments. Analysis of the adsorption data using the ideal adsorption solution theory revealed the potential use of these materials in CO<sub>2</sub>/CH<sub>4</sub> separation applications.

# 1 Introduction

## 1.1 Porous materials

Porous materials became very popular the past decades in the field of chemistry due to their structural and functional applications. Porous matter exhibits essential high surface area, highly valued for use in reactions at surfaces such as catalysis,<sup>[1]</sup> adsorption for gas capture, separation and storage,<sup>[2],[3],[4]</sup> as scaffolds for tissue engineering<sup>[5]</sup> and drug delivery.<sup>[6]</sup> Due to the existence of the pores, porous materials have different properties compared to the bulk materials, including their optical, electronic and chemical/physical behavior. The pore morphology can be either random or regular resulting in disordered or ordered pore systems, respectively. Based on the pore diameter porous materials are divided into three main categories, microporous ( $D < 2$  nm), mesoporous ( $D = 2 - 50$  nm) and macroporous ( $D > 50$ nm).<sup>[7],[8]</sup> Porous materials can also be classified according to their framework into inorganic porous materials, organic porous materials and hybrid (organic-inorganic) porous materials.

Zeolites are a class of crystalline inorganic microporous materials with large surface areas, narrow pore-size distributions and high ion exchange properties that render them excellent candidates for heterogeneous catalysis and gas sorption applications. Zeolite membranes have been reported<sup>[9],[10]</sup> to exhibit  $\text{CO}_2/\text{CH}_4$ ,  $\text{H}_2/\text{CH}_4$  and  $\text{CO}_2/\text{N}_2$  separation selectivities up to 171, 32 and 20, respectively. Zeolite membranes display drastic improvements in gas separation properties compared to commercially available polymeric membranes.<sup>[11]</sup>

Organic-inorganic hybrids such as metal-organic framework materials (MOFs) have attracted extensive attention lately since they have shown promising results in a wide range of applications such as gas storage, chemical separations, chemical sensing, catalysis, ion exchange, light harvesting and drug delivery. MOFs are ordered microporous materials built by linking the inorganic part, mostly transition metals and lanthanoid ions with various coordination numbers, using bi- or multifunctional organic linkers. Interactions between the inorganic part and the organic linker are coordinative or ionic non covalent as in zeolites. These materials exhibit exceptionally high surface areas and the dimensions and shape of the channels can be easily tuned by changing the organic linkers. Metal organic framework



adsorbents functionalized with dual amines and with linear polyethylene-imine (PEI) incorporated within the amine pores have been reported with a remarkable CO<sub>2</sub>/CH<sub>4</sub> selectivity up to 931 at 25°C and 0.5 bar, whereas the BET N<sub>2</sub> surface area was dramatically low at 96.4 m<sup>2</sup> gr<sup>-1</sup> which suggests that some pores are not accessible.<sup>[12]</sup> These results indicate that the incorporation of the amine groups into the materials is far more efficient than the covalent grafting. Metal-organic materials without amino groups have also been reported<sup>[13]</sup> that exhibited CO<sub>2</sub>/CH<sub>4</sub> and CO<sub>2</sub>/N<sub>2</sub> IAST selectivities up to 33 and 140, respectively at 298K and 1 bar. These results were attributed to the increase of the isosteric heat of adsorption due to better overlap of the attractive fields in the narrow pores (5.15 Å). This material afforded a BET apparent surface area of 735 m<sup>2</sup> gr<sup>-1</sup> from N<sub>2</sub> adsorption measurements which was not high with respect to other MOF materials that have BET surface areas up to 7000 m<sup>2</sup> gr<sup>-1</sup>.<sup>[14]</sup> These results suggest that high surface area material is not necessarily efficient for gas separation applications. Functional groups (such as amines) and metal ions also play a key role in the enhancement of the gas selectivity of porous materials.

## 1.2 Porous polymers

Organic porous polymers are an important subset of porous materials. Porous polymers raised a lot of attention lately due to several advantages they possess such as ease of synthesis and facile processing to form various polymeric structures such as monoliths, beads, films, etc that exhibit high surface areas and well-defined porosities. Porous polymers can be synthesized using a variety of polymerization techniques such as polycondensation, high internal phase emulsion, post-crosslinking method, suspension polymerization or emulsion polymerization (emulsifier-free, mini emulsion). Post polymerization crosslinking is known as a technique that enables the preparation of high surface area porous materials from various polymers by creating additional porosity and collapse resistance after drying. Microporous organic polymers with certain properties including large surface area, narrow pore size distribution, and high chemical and thermal stability are excellent candidates for potential applications in gas capture and separation. There are a few classes of microporous organic polymers (MOPs), including hypercrosslinked polymers (HCPs),<sup>[15]</sup> polymers of intrinsic microporosity (PIMs),<sup>[16]</sup> conjugated microporous polymers (CMPs) and covalent organic frameworks (COFs).<sup>[17]</sup> Hypercrosslinked

polymers are among the most popular porous polymeric materials. They are usually synthesized through a two step process (post-crosslinking method). First, linear chains of the main polymer (styrene is very popular) are synthesized and then a crosslinker is used to further crosslink these chains. Thus, these types of materials exhibit high surface area, high porosity in the range of micro/meso porous materials and significant gas capture properties (usually tested for CO<sub>2</sub> and H<sub>2</sub>). Hyper-cross-linked materials are known to be suitable for sorption separation of small molecules, thus they are widely used for gas capture, gas storage and catalyst support.<sup>[15]</sup>

Porous polymers with pores in the micropore range can be synthesized within high internal phase emulsions (HIPEs) and these porous emulsion templated polymers are known as polyHIPEs.<sup>[18],[19]</sup> HIPEs are highly viscous emulsions with the major phase dispersed as discrete droplets within the continuous minor phase. A typical polyHIPE porous structure is that of the cross-linked styrene-*co*-divinylbenzene copolymer. This type of polyHIPE was synthesized via free radical initiated post polymerization cross-linking of styrene-*co*-DVB and monolithic polyHIPEs with surface areas up to 355 m<sup>2</sup>/g and new pores mostly in the mesopores region were obtained. For the post polymerization cross-linking reaction unreacted vinyl groups which remained on the polymer after the termination of the standard polymerization were employed.<sup>[20]</sup>

### 1.3 Porphyrins and Metalloporphyrins

The word porphyrin has its origin in the Greek word porphura that means purple. They are highly colored pigments that are either naturally found in biological organisms or chemically synthesized. Porphyrins are organic aromatic macrocyclic compounds with their basic structure consisting of four pyrrole rings linked with four methine bridges forming their center ring (**Figure 1.1**).<sup>[21]</sup>

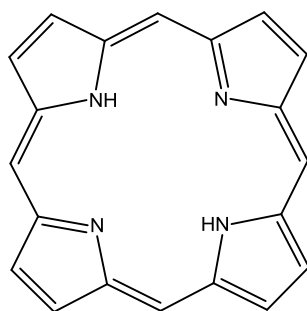


**Figure 1.1** Basic structure of porphyrin.

Porphyrins and metalloporphyrins have attracted considerable attention the last few decades due to their outstanding physicochemical properties and applications in diverse fields. The central aromatic ring is the reason why porphyrins exhibit many important properties, such as absorption, emission, extended p-network and charge transfer, thus finding numerous applications in oxygen binding, electron transfer, catalysis, light harvesting, optoelectronic devices, photo-dynamic therapy and gas storage/separation. Although the porphyrin ring is a macromolecule, it is highly flexible and a number of structural changes involving different central metal ions and peripheral substituents can be introduced without compromising its excellent chemical and thermal stability, thus increasing its range of applications.

### **1.3.1 Porphyrin-containing polymers**

Recently, much research effort has been devoted to the design and synthesis of porphyrin-containing polymers. Porphyrin and metalloporphyrin units can be incorporated into polymer chains by three ways known so far; (i) bound onto the main polymer chain as pendant groups, (ii) as part of the backbone of the main polymer network<sup>[22]</sup> and (iii) as the central group in dendrimers or star polymers.<sup>[23]</sup> These materials have been also proposed for use in catalysis and gas storage/separation applications.<sup>[24]</sup>

Star polymers have been successfully synthesized using a porphyrin initiator core via atom transfer radical polymerization of styrene and various alkyl acrylates and methacrylates.<sup>[25]</sup> Furthermore, the resultant polymers were successfully metalated using appropriate metal salts (PdCl, ZnBr or CuBr) and were investigated by UV-vis and fluorescence spectroscopy. In another study, click polymerization reactions for the production of porphyrin-containing polymers have been reported.<sup>[22]</sup> These reactions are promising since they are efficient, reliable and theoretically can produce polymers with high molecular weights. The polymers were soluble in common organic solvents and stable at temperature up to 350°C. The synthesis of porphyrin-containing polymers by polycondensation polymerization between two different functional groups incorporated into a porphyrin molecule and another monomer has been also reported. This method is effective but there is an important drawback; almost all coupling reactions must be performed using rigorously anhydrous solvents under inert atmospheres, thus limiting the flexibility, scale-up and functionality of the reaction. Furthermore the purification process of the final polymer is challenging due

to the produced by-products. For these reasons other synthetic routes have been explored. As a result, porphyrin-containing polymers have been synthesized using chain polymerization of methacrylate-functionalized porphyrin monomers.

## 1.4 Gas sorption

In the past few decades environmental issues have attracted great research attention due to climate changes, global warming and the limitation of energy resources. The total CO<sub>2</sub> concentration in the atmosphere is increasing rapidly since 1800 due to the industrial revolution, thus the development of novel materials with high adsorption selectivity towards CO<sub>2</sub> over CH<sub>4</sub>, H<sub>2</sub> or N<sub>2</sub> is crucial in order to stabilize atmospheric CO<sub>2</sub> levels and prevent global warming.<sup>[26]</sup> Moreover, natural gas and biogas are very promising solutions for the energy power problem both environmentally and economically. It can be produced from various waste sources, including landfill material; animal manure; wastewater; and industrial, institutional, and commercial organic waste. Biogas can also be produced from other lignocellulosic biomass (e.g., crop and forest residues, dedicated energy crops) through dry fermentation, co-digestion, or thermochemical conversions (e.g., gasification). Biogas can be combusted to provide heat, electricity, or both. This upgraded biogas is comparable to the conventional natural gas, and thus can be injected into the pipeline grid or used as a transportation fuel in a compressed or liquefied form.

However, carbon dioxide is a major impurity in natural gas, biogas and other gas streams. Biogas is usually 50% to 80% methane and 20% to 50% carbon dioxide, with traces of other gases such as hydrogen, carbon monoxide, and nitrogen. Also, natural gas is usually more than 70% methane, with traces of carbon dioxide and other hydrocarbon (such as propane and butane) contaminants. Purification of biogas from CO<sub>2</sub> is mandatory since CO<sub>2</sub> reduces its energy content and leads to the corrosion of natural gas pipelines. In addition, renewable natural gas, also called biomethane, is produced from biogas and is becoming more common as a vehicle fuel. With minor cleanup, biogas can be used to generate electricity and heat. When processed to a higher purity standard, biogas is called RNG and can be used as an alternative fuel for natural gas vehicles. Furthermore, hydrogen mainly produced by steam reforming of natural gas can be used as a clean fuel in fuel cells. The synthetic gas produced by this

process contains impurities like CO<sub>2</sub> and CH<sub>4</sub> that need to be removed before hydrogen can be used effectively.

New, cost-effective, advanced technologies for CO<sub>2</sub> separation are continually being investigated, designed and developed. Porous materials relying on physical adsorption are promising candidates for CO<sub>2</sub> capture due to their low regeneration energy consumption and high CO<sub>2</sub> sorption capacity.<sup>[27]</sup> Physisorption is preferable over chemisorption, since it does not require exchange of chemical bonds limiting the kinetic barrier and the heat generation. Physisorption of the gas molecules with the adsorbent surface is achieved through van der Waals interactions. The progress of CO<sub>2</sub> separation and capture from a gas mixture (CO<sub>2</sub>/CH<sub>4</sub>, CO<sub>2</sub>/H<sub>2</sub> and CO<sub>2</sub>/N<sub>2</sub>) is mainly developed from the chemical conversion point of view with the CO<sub>2</sub>/CH<sub>4</sub> separation being the least investigated so far. There are many researched fields for CO<sub>2</sub> separation which include adsorption, absorption, membrane separation and biotechnology. An important parameter to consider is the cost of gas purification especially when the process is taken to an industrial level. A way to limit the cost is to reduce the amount of energy required by using materials that are effective close to atmospheric pressure and room temperature.<sup>[28]</sup> The evaluation of the pore structure of the porous materials developed is an important aspect in the process of their design and application for gas separation.

Gas adsorption is widely used for determining the porous structure of porous materials. The main areas of interest in understanding the porous structure are the overall porosity (pore volume divided by total sample volume), average pore size and surface area (surface characteristics). Adsorption occurs whenever a solid surface is immersed in or exposed to a liquid or gas and can be defined as the enrichment of one or more components in an interfacial layer, or increase in density of the fluid in the vicinity of an interface. The gas used is called the adsorbate, while the material present in the solid phase may be distinguished as the adsorbent.<sup>[29]</sup> The adsorption process is usually studied through an adsorption isotherm and several theories (Langmuir, BET, DR etc) are employed for its analysis. The quantity adsorbed is nearly always normalized by the mass of the adsorbent to allow comparison of different materials. Nitrogen and carbon dioxide adsorption analysis is used for the characterization of the porous materials synthesized in the present work.

### 1.4.1 Porous materials for gas sorption

Porous materials are mainly characterized by their surface area, porosity and potential gas adsorption. Porous network polymers have been synthesized via dioxane formation resulting to BET surface areas of 1000 m<sup>2</sup>/gr.<sup>[30]</sup> Polyporphyrins were also synthesized reaching surface areas as high as 1522 m<sup>2</sup>/g and hydrogen uptake measurements revealed a slight increase in heat of adsorption after the insertion of Fe(II) ions into the porphyrin rings.<sup>[31]</sup> In another study, nanoporous nickel-doped porphyrin polymers were synthesized through coupling reactions and exhibited BET surface areas up to 1711 m<sup>2</sup>/gr. Their adsorption selectivity for carbon dioxide over nitrogen and methane was investigated based on single gas sorption isotherms resulting to selectivities of 19.1 and 4.22, respectively.<sup>[24]</sup>

### 1.4.2 Types of adsorption isotherms

Two types of adsorption isotherms have been identified; physical and chemical isotherms. Adsorption isotherms, mainly resulting from physisorption, have a variety of forms and the majority of them can be grouped into one of the six types classified by IUPAC. The first five types (I to V) are referred as the Brunauer classification. The IUPAC classification (1985) introduced a more recent type of physisorption isotherm (type VI) (Figure 1.2a).<sup>[32]</sup>

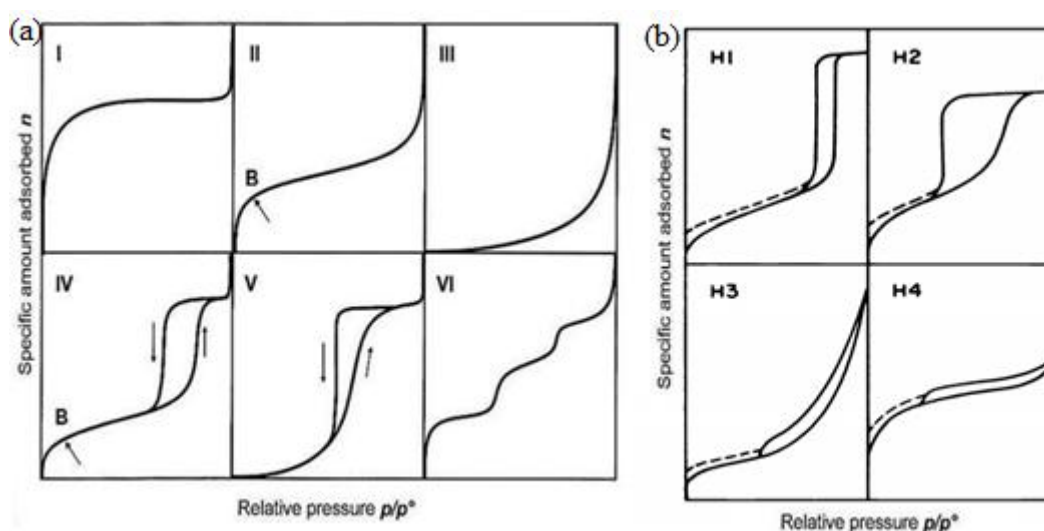


**Figure 1.2** (a) The six main types of adsorption isotherms and (b) the four types of hysteresis loops based on the IUPAC classification.

Type I isotherm is concave to the relative pressure ( $p/p^0$ ) axis. The isotherm curve rises sharply at low relative pressure range until it reaches a plateau when the  $p/p^0$  goes to 1. The narrow range of relative pressure required to obtain this plateau is an indication of a limited range of pore size. Plus the horizontal appearance of the plateau depicts a small external surface area. As a result the limiting adsorption is dependent on the available micro-pore volume.

Type II isotherm is at the beginning concave to the relative pressure ( $p/p^0$ ) axis, then becomes linear and at high pressure close to 1 is convex to the ( $p/p^0$ ) axis. This formation indicates the presence of an adsorbed layer with progressively increasing thickness. If the knee of the isotherm is sharp, the uptake at point B (the beginning of the linear section) is considered to represent the completion of the monolayer and the beginning of the multilayer. These types of isotherms are obtained for non-porous or macro-porous adsorbents that allow unrestricted monolayer-multilayer adsorption and complete reversibility of the adsorption-desorption isotherm (absence of hysteresis).

Type III isotherm is convex to the relative pressure ( $p/p^0$ ) axis over the complete range, therefore has no point B. These isotherms are not common since they are assigned to weak adsorbent-adsorbate interactions.

Type IV isotherm is at the initial region very similar to the type II but tends to level off at a small plateau at high relative pressures. It exhibits a hysteresis loop that is usually associated with the filling and emptying of the mesopores by capillary condensation. The lower branch represents measurements obtained by progressive addition of gas of the adsorbent whereas the upper branch by progressive withdrawal. Type IV isotherms are very common but the hysteresis loops vary according to each system and can be categorized in four types (**Figure 1.2b**).

Type V isotherm is convex to the relative pressure ( $p/p^0$ ) axis at the first part and levels off at high relative pressure. As type III these isotherms are very rare. This isotherm type is associated with weak adsorbent-adsorbate interactions and the hysteresis loop is formed according to pore filling and emptying mechanisms.

Type VI isotherm is also relatively rare and it is also known as stepped isotherm. It is associated with layer-by-layer adsorption on a highly uniform surface. The sharpness of the steps is dependent on the system and the temperature.

Hysteresis loops are associated with capillary condensation and they usually are distinctive and reproducible for meso-porous systems. There are many different forms of loops reported in the literature but are all mainly classified into four major

categories according to the IUPAC classification. Type H1 is a narrow loop with perpendicular and nearly parallel adsorption- desorption branches. This type of loop is obtained from systems with a narrow distribution of uniform pores. Type H2 loop is very broad with a long nearly flat plateau and a steep desorption branch. H2 loops are obtained from materials with a complex pore structure that exhibit interconnected pore networks of different size and shape. Type H3 and H4 loops are very similar since both do not terminate in a plateau at high relative pressure. They are usually obtained by aggregates of particles or adsorbents containing slit-shaped pores but in H4 loops the pore size distribution is mainly attributed to micro-pores.

### 1.4.3 Gas adsorption theory

The Brunauer-Emmett-Teller (BET)<sup>[33]</sup> gas adsorption theory is the foundation for the measurement of surface area in high specific surface materials. Brunauer et al. derived an isotherm for the adsorption of multimolecular layers of gas on a solid adsorbent similar to Langmuir's derivation for a uniform molecular layer. Surface area is determined using equation [1.1]

$$\frac{P}{V_{ads} (P_0 - P)} = \frac{1}{V_m c} + \frac{c - 1}{V_m c} \frac{P}{P_0} \quad [1.1]$$

, where  $P$  is the applied pressure,  $P_0$  is the saturation pressure,  $V_{ads}$  is the volume of gas adsorbed at  $P/P_0$ ,  $V_m$  is the volume of adsorbate for one monolayer of surface coverage, and  $c$  is related to the heat of adsorption in the first and subsequent adsorbed layers. Plots of  $P/(V_{ads} (P_0 - P))$  versus  $P/P_0$  yield a straight line, from which the slope and intercept can be used to determine  $V_m$  and  $c$ . The surface area  $A_s$  of the specimen is

$$A_s = \frac{V_m}{V_{molecule}} A_{molecule} \quad [1.2]$$

, where  $V_{molecule}$  is the volume of the adsorbate molecule, and  $A_{molecule}$  is the cross-sectional area of the adsorbate molecule.

The Dubinin–Radushkevich (DR) equation is widely used to describe adsorption of sub-critical vapours in microporous solids such as activated carbons and zeolites. Dubinin was the first to introduce the idea of micropore filling. In 1947 Dubinin and Radushkevich formulated the following equation for the characteristic curve in terms of the fractional filling,  $W/W_0$ , of the micropore volume,  $W_0$ ,



$$\frac{W}{W_0} = \exp \left[ - \left( \frac{A}{E} \right)^2 \right] \quad [1.3]$$

, where A is an adsorption affinity  $A = -RT \ln(p/p^o)$  [1.4] and E is a characteristic energy for the given system. The combination of equations [1.3] and [1.4] results to the isotherm equation of the DR theory. With the introduction of a scaling factor,  $\beta$ , it becomes:

$$\frac{W}{W_0} = \exp \left\{ - \frac{[RT \ln(p^o/p)]^2}{(\beta E_0)^2} \right\} \quad [1.5]$$

, where  $E_0$  is a characteristic energy.

Rearranging the [1.5] equation gives the DR equation in its usual form [1.6]

$$\log_{10} \left[ \frac{W}{W_0} \right] = -D \log_{10}^2 \left( \frac{p^o}{p} \right) \quad [1.6]$$

where  $D=0.434B(T/\beta)^2$  and B is the structural constant ( $B=5.304(R/E_0)^2$ ).<sup>[34],[35],[36],[37]</sup>

#### 1.4.4 DFT method for pore size distribution

The density functional theory was first proposed by Seaton et al. in 1989 in order to solve the problem of pore analysis via the BET method which fails to detect different pore structure morphologies, to report effects of microporosity and to predict pore sizes. Adsorption isotherms can be analyzed through the DFT model in order to determine the pore size distribution of the material investigated. Taking the DFT model one step further, the non-local DFT method was developed initially for simple slit geometries for activated carbons but was rapidly escalated taking under consideration more pore morphologies and structures and typical adsorbates. The NLDFT theory deliberates the complexity of the hysteresis loop of the adsorption isotherms related to physical phenomena such as, (i) inherent metastability of confined fluid, (ii) pore blocking, (iii) network effects, (iv) instability of adsorbed films and (v) cavitation of condensed fluid, that relate to the geometrical characteristics of a pore structure.<sup>[38],[39]</sup> Currently there is a large library available with various DFT kernels for specific applications.

In order to employ the non-local DFT model several assumptions regarding the adsorbent and the adsorbate have been made. Firstly, the equilibrium distribution of the adsorbate in the pores corresponds to the potential minimum adsorption presented the density of the adsorbed fluid. Secondly, the solid adsorbent is considered as inert

and non-deformable during the adsorption. Furthermore, the adsorption interactions of the adsorbent and the adsorbate are modeled with an effective solid-fluid spatially distributed potential  $U_{\text{ext}}(\mathbf{r})$ . Based on these assumptions the equilibrium adsorption state, for a given fluid chemical potential  $\mu_f$  is determined in the NLDFT method by minimizing the grand potential  $\Omega_f$  of the fluid in the pore and subjected to the external potential  $U_{\text{ext}}$  [1.7].

$$\Omega_f[\rho_f(\mathbf{r})] = F_f[\rho_f(\mathbf{r})] - \int d\mathbf{r} \rho_f(\mathbf{r}) [\mu_f - U_{\text{ext}}(\mathbf{r})] \quad [1.7]$$

, where  $\mathbf{r}$  is the position vector inside the pore,  $\rho_f(\mathbf{r})$  is the fluid density and  $F_f$  is the Helmholtz free energy of the fluid.

The latter is expressed as a summary of the ideal term  $F_{id}[\rho_f(\mathbf{r})]$ , the excess hard sphere (HS) repulsion term  $F_{ex}[\rho_f(\mathbf{r})]$  and the attractive term given by the equation [1.8],

$$F_f[\rho_f(\mathbf{r})] = F_{id}[\rho_f(\mathbf{r})] + F_{ex}[\rho_f(\mathbf{r})] + \frac{1}{2} \iint d\mathbf{r} d\mathbf{r}' \rho_f(\mathbf{r}) \rho_f(\mathbf{r}') u_{ff}(|\mathbf{r} - \mathbf{r}'|) \quad [1.8]$$

, where  $u_{ff}(\mathbf{r})$  is the attractive part of the pairwise fluid-fluid potential.

The physical adsorption of gases like nitrogen, argon and carbon dioxide is used for the pore structure characterization of a material. The pore size distribution is extracted from the experimental adsorption isotherm  $N_{\text{exp}}(P/P_0)$  solving the integral adsorption equation [1.9],

$$N_{\text{exp}}(P/P_0) = \int_{D_{\text{min}}}^{D_{\text{max}}} N_{\text{NLDFT}}(P/P_0, D) f(D) dD \quad [1.9]$$

, where  $f(D)$  is the pore size distribution function,  $D_{\text{min}}$  is the minimum  $D_{\text{max}}$  = maximum pore sizes in the DFT kernel.

The pore width in the NLDFT kernels is determined as the center-to-center distance between the outer layers of adsorption centers on the opposite pore walls. The DFT kernels were built for calculating pore size distribution from adsorption isotherms using different adsorbates such as nitrogen at 77 K, argon for 77 and 87 K and carbon dioxide at 273 K. However, the results of pore size distributions for the same material obtained using different adsorbates have not severe differences. Nitrogen is the most common adsorbate for adsorption characterization techniques but for microporous materials argon and carbon dioxide are more suitable. At very low pressures the pore filling of the ultramicropores of the network takes place for both nitrogen and argon adsorption, but for low pressures the problem of restricted

diffusion appears, preventing the gas molecules from entering the narrowest micropores of width below 0.45 nm. For the solution of this important problem, CO<sub>2</sub> at 273K is mainly used as the adsorbate for characterizing ultramicropore materials, since the higher temperature and the smaller size of the CO<sub>2</sub> molecules results to better diffusion.<sup>[40]</sup>

### 1.4.5 Ideal Adsorbed Solution Theory (IAST)

Gas selectivity was predicted using the ideal adsorbed solution theory (IAST). The single-component adsorption isotherms were described by fitting the data with the virial-type equation **[1.10]**<sup>[41]</sup>:

$$p = \frac{V}{K} \exp(c_1 v + c_2 v^2 + c_3 v^3 + c_4 v^4) \quad \mathbf{[1.10]}$$

, where p the pressure (Torr), v is the adsorbed amount (mmol/gr), K is the Henry constant (mmol/gr Torr) and c<sub>i</sub> are the constants of virial equation. The free energy of desorption for a specific value of temperature and pressure of the gas is obtained from the analytical integration of equation **[1.11]**:

$$G(T, p) = RT \int_0^p \frac{n}{p} dp = RT \left( v + \frac{1}{2} c_1 v^2 + \frac{2}{3} c_2 v^3 + \frac{3}{4} c_3 v^4 + \frac{4}{5} c_4 v^5 \right) \quad \mathbf{[1.11]}$$

The free energy of desorption is a function of temperature and pressure, G(T,p), and described the minimum work (Gibbs free energy) that is required to completely degas the adsorbent surface. For a binary mixture of components, i and j, equation **[1.11]** yields the individual pure loadings v<sub>i</sub><sup>0</sup> and v<sub>j</sub><sup>0</sup> at the same free energy of desorption:

$$G_i^0(v_i^0) = G_j^0(v_j^0) \quad \mathbf{[1.12]}$$

The partial pressures of components i and j in an ideal adsorption mixture are given by the equations **[1.13]** and **[1.14]**:

$$p y_i = p_i^0(v_i^0) x_i \quad \mathbf{[1.13]}$$

$$p y_j = p_j^0(v_j^0) x_j \quad \mathbf{[1.14]}$$

, where y<sub>i</sub>(= 1 - y<sub>j</sub>) and x<sub>i</sub>(= 1 - x<sub>j</sub>) are the molar fractions of the component i in the gas phase and the adsorbed phase, respectively, and p<sub>i</sub><sup>0</sup>, p<sub>j</sub><sup>0</sup> is the pure component pressure of i and j, respectively. After solving the equations **[1.12]**-**[1.14]** and the equation **[1.10]**, the selectivity for the adsorbates i and j (s<sub>i,j</sub>) and the total pressure (p) of the gas mixture were obtained from equations **[1.15]** and **[1.16]**, respectively.

$$s_{i,j} = \frac{x_i/y_i}{x_j/y_j} = \frac{p_j^0}{p_i^0} \quad [1.15]$$

$$p = \sum_i^j p_i^0 x_i \quad [1.16]$$

The gas adsorption isotherms acquired at different temperatures (263K and 273K) can be described and analyzed using the virial-type equation [1.17]:

$$\ln p = \ln v + \frac{1}{T} \sum_{i=0}^m a_i v_i + \sum_{i=0}^m b_i v^i \quad [1.17]$$

, where p the pressure in Torr, v is the amount adsorbed in mmol/gr, T is the temperature in K, and  $a_i$ ,  $b_i$  are the adjustable parameters. The m and n represent the order of polynomials that are required to adequately describe the isotherms. The coverage-dependent isosteric heat of adsorption,  $q_{st}$ , is calculated by using the expression [1.18]:

$$q_{st} = -R \sum_{i=1}^m a_i v_i \quad [1.18]$$

, where R is the universal gas constant.

## 1.5 Emulsion polymerization

Emulsion polymerization <sup>[42],[43]</sup> is a unique chemical process that is widely used for the synthesis of many polymeric materials. It is a complex system of radical addition to a growing polymeric chain that proceeds in a heterogeneous environment leading to a colloidal suspension.<sup>[44]</sup> Emulsion polymerization comprises a water-insoluble monomer(s), a water-soluble initiator, a dispersion medium and potentially a surfactant. Emulsion polymerization is a very popular method that offers many kinetic and technological advantages over other free radical polymerization methods (bulk, suspension, solution); therefore it is widely used in an industrial scale for the production of emulsion paints, adhesives, rubbers, coatings and sealants.

Flexibility is the key word in emulsion polymerization. Various monomers, processing methods and additives can be used making the process highly flexible. A wide variety of materials with specialized properties can be manufactured, tailoring properties, such as particle size, composition, morphology, and molecular weight. The rate of polymerization increases as the number of particles increases. Thus, the

molecular weight of the polymer is proportional to the initial radicals added to the solution. High molecular weight polymers can easily and rapidly be obtained due to fast polymerization rates.

Emulsion polymers are colloids, meaning that they consist of small, discrete particles dispersed in a continuous liquid media. Colloids have many unique and interesting properties as a result of their small size (typically less than 1  $\mu\text{m}$ ) and large interfacial area. When monomer droplets of polymer particles are dispersed in water there is an associated increase in free energy at the interface between the colloidal particles and the continuous phase. The interfacial free energy increase is substantial in colloids with small sizes and large interfacial areas. The minimization of interfacial free energy is thermodynamically favorable, and provides a strong driving force for coagulation/aggregation. Such results are undesirable and ways to introduce colloidal stability in the system against aggregation are necessary. A surfactant is used for this purpose. Surfactants are surface active agents with a hydrophilic head group and a hydrophobic tail group. They are classified according to the nature of the head group and can be either anionic or cationic resulting to electrostatic stabilization of the system or non-ionic that sterically stabilizes the system (**Figure 1.3**). The steric stabilization mechanism involves absorbed or grafted polymer chains at the surface of the latex particles.

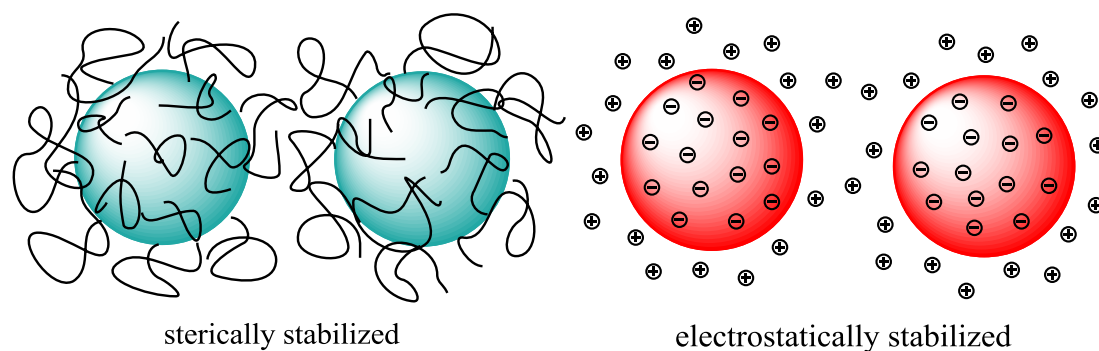


**Figure 1.3** Schematic representation of sterically and electrostatically stabilized colloidal particles

The electrostatic stabilization mechanism involves latex particles with a surface charge and a corresponding layer of ions of opposite charge that form the electrical double layers (EDL). This is effective in aqueous or polar solvents in which surface ionization can occur, creating EDL layers (**Figure 1.4**).

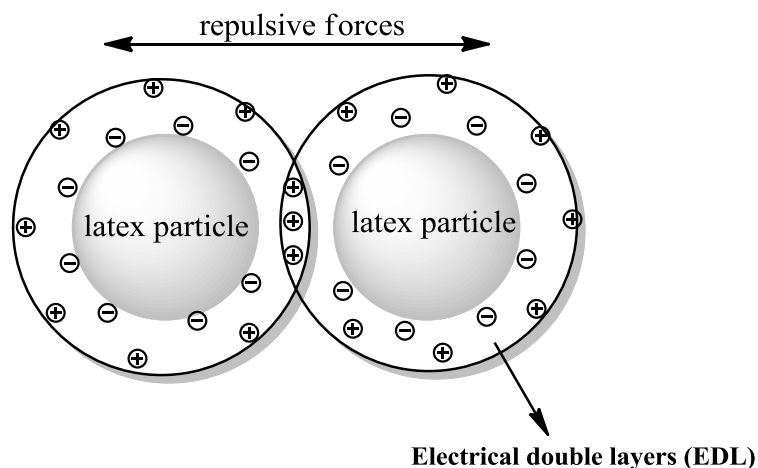


**Figure 1.4** Schematic representation of the electrical double layers and the electrostatic stabilization mechanism.

The surfactant plays another important role in emulsion polymerization besides stabilization. It is critically involved in the nucleation mechanism of the polymer particles. The amount of surfactant used allows control over the particle size distribution. As the free surfactant concentration in the water phase increases, it reaches a point at which no additional surfactant is soluble. This point is known as the critical micelle concentration (CMC). Any surfactant added after the CMC has been reached, will associate into aggregates called micelles. The cores of the micelles are hydrophobic and attract monomer from the stabilized droplets, thereby swelling the micelles. Radicals generated by the initiator react with monomer dissolved in the water phase to form oligoradicals. Once the oligoradicals reach a critical chain length, they can either aggregate to form primary particles by homogeneous nucleation or enter monomer-swollen micelles to form primary particles by micellar nucleation.

In order for the polymerization to start an initiator is required. The function of the initiator is to generate free radicals that lead to the propagation of the polymer molecules. The free radicals can be produced either by thermal decomposition or by redox reactions. The most commonly used water-soluble initiators are persulfates for example, potassium or ammonium persulfate. Persulfate ion decomposes thermally in the aqueous phase to give two sulfate radical anions which can initiate the polymerization. Oil-soluble compounds such as benzoyl peroxide and azobisisobutyronitrile (AIBN) can be employed as thermal initiators in emulsion polymerizations. Another initiation system consists of redox initiators (such as

persulfate-bisulfate system) which produce free radicals through an oxidation-reduction reaction at relatively low temperatures.<sup>[45]</sup>

The mechanism for the formation of the polymer particles proceeds through two simultaneous processes. First the entry of the radicals from the aqueous solution into the micelles (micellar nucleation) and second the oligomeric radicals formed into the solution becoming insoluble and precipitate forming polymer nuclei (homogeneous nucleation). Lower water solubility and higher surfactant concentration favor micellar nucleation. In emulsion polymerization, the dispersion medium, for monomer droplets and polymer particles, is generally water but this does not mean that other solvents are mandatory. Water is inexpensive, nonflammable, nontoxic, inactive and environmentally friendly. It provides excellent heat transfer and low viscosity. It also acts as the medium of transfer for monomer units from droplets to particles, the place of initiator decomposition and oligomer formation. The aqueous continuous phase has a high heat capacity; therefore allows efficient removal of the heat generated during the polymerization. Water also allows the final latex polymer to maintain a low viscosity.

Copolymerization can occur easily using this emulsion polymerization but the resulting copolymer is usually random. There are also some disadvantages when using emulsion polymerization. The presence of surfactants and other ingredients in the final polymer constitutes unavoidable contamination since they remain in the polymer and the cleaning process requires further additional operations. For obtaining dry polymers water removal is a very energy-intensive process. Chain transfer is a very common unavoidable reaction in emulsion polymerization due to high amount of monomers.<sup>[46]</sup>

The final latex particle size is tuned by various factors such as the reaction temperature, the stirring rate, the monomer type and concentration, the initiator type and concentration and the overall ionic strength.

### **1.5.1 Emulsion polymerization intervals**

Emulsion polymerizations are free radical processes. There are three steps in the free radical polymerization mechanism: initiation, propagation and termination. The process of emulsion polymerization can be described by three intervals according to the theories proposed by Harkins and Smith and Ewart, the nucleation, the particle

growth and the completion stage (**Figure 1.5**). Interval I (*nucleation stage*) is the initial stage where the particle formation takes place. During this stage an initiator compound generates free radicals by thermal decomposition while the water-insoluble monomer molecules are concentrated in a large monomer droplet. The free radicals initiate polymerization by reacting with a monomer molecule forming oligomers. Because initiator molecules constantly decompose to form radicals, new chains are also constantly formed. The oligomers formed diffuse into the micelles initiating the particle growth. In addition, monomers diffuse from the large monomer droplet to the empty or semi-empty micelles. The number of particles and the rate of polymerization both increase as new particles are formed. As surfactant units are used to stabilize new particles, the free surfactant concentration falls below the critical micelle concentration, and nucleation ends. The number of particles is constant after this point and the empty micelles disappear (**Figure 1.5b**).

During Interval II (*the particle growth stage*), the existing particles continue to polymerize and consume the monomer units contained in the large monomer droplets. The monomer is transported through the aqueous phase, as the result of a concentration gradient, to the site of polymerization (i.e., the growing polymer particles). The polymer particles contain all the unreacted monomer and essentially all of the emulsifier molecules are also attached to the surface of polymer particles (**Figure 1.5c**). At the end of Interval II, the monomer in the droplets is depleted, and no monomer droplets are present thereafter.

Finally during Interval III (*the completion stage*), the monomer already contained in the polymer particles polymerizes until it is fully converted to polymer (**Figure 1.5d**). The concentration of monomer in the polymer particles drops to essentially zero. The system now comprises a dispersion of polymer particles stabilized with the molecules of the surfactant (**Figure 1.5e**).



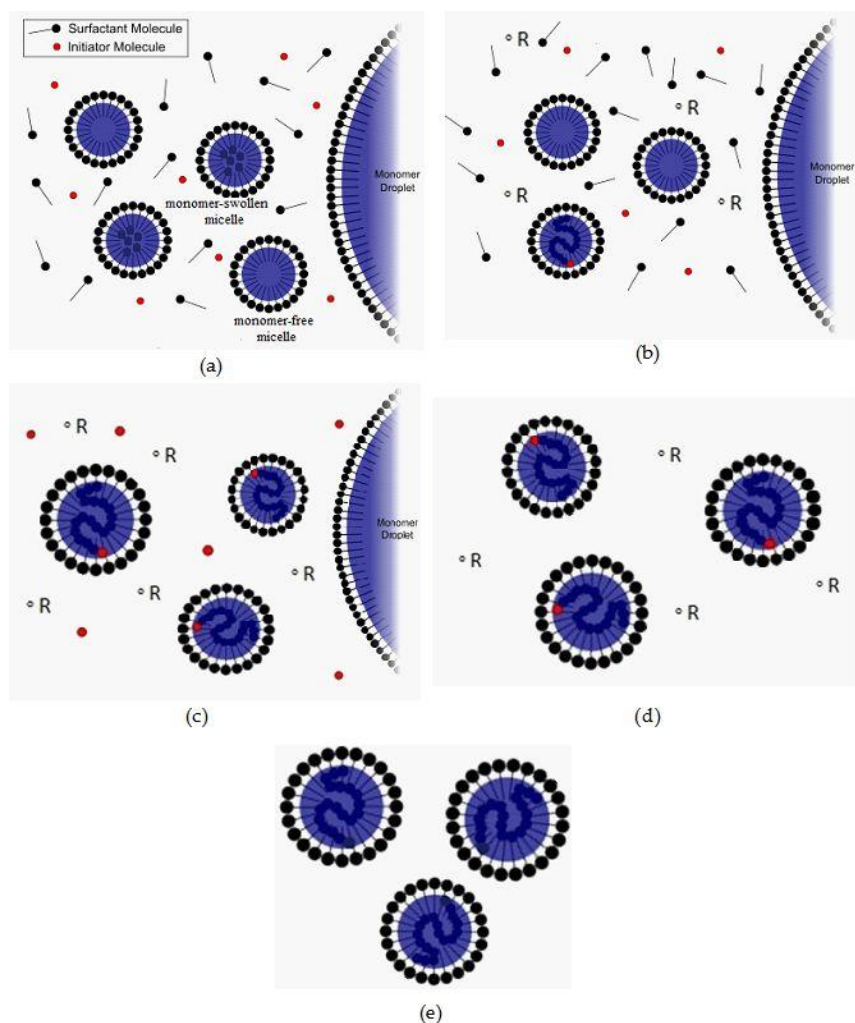


**Figure 1.5** Schematic representation of the emulsion polymerization mechanism (intervals) (a-e).

## 1.6 Current study

Lately, interest in porous materials for gas purification and gas capture has highly increased. In response to this, the present work provides a simple and facile process to produce highly cross-linked particles that exhibit a sufficient internal surface area and are potential candidates for use in the separation of carbon dioxide from methane gas. This work focuses on the synthesis of highly cross-linked porphyrin-containing colloidal particles by a typical free-radical emulsion copolymerization process.

The particles were based on a highly cross-linked polystyrene network containing porphyrin moieties. The cross-link density was regulated by progressively increasing the porphyrin content of the particles. In order to incorporate the porphyrin moieties inside the polymer network a tetra-methacrylatefunctionalized porphyrin molecule

was prepared by reaction of the tetra-hydroxy porphine with methacryloyl chloride. The successful preparation of the tetra-methacrylatefunctionalized porphyrin (PO) was confirmed by  $^1\text{H-NMR}$  spectroscopy.

The functionalized porphyrin (PO) was then used as a cross-linker in the emulsion copolymerization of styrene (S) and divinylbenzene (D) resulting to the PO-S-D porous nanoparticles. The size and the morphology of the PO-S-D nanoparticles were examined using DLS measurements and were confirmed by SEM and TEM imaging. The PO content of the particles was investigated by UV-VIS spectroscopy.

In order to obtain solvent-free open porous samples a supercritical point drying process was employed. The samples were dispersed either in EtOH or in DMF to examine the effect of the solvent on the particle swelling and porosity. The internal surface area and pore size of the porous network was investigated using  $\text{N}_2$  and  $\text{CO}_2$  adsorption-desorption measurements. Finally, the separation performance of  $\text{CO}_2$  over  $\text{CH}_4$  of the porous particles was inspected by the  $\text{CO}_2$  and  $\text{CH}_4$  single-component isotherms in various temperatures and pressures and the selectivity was determined using the IAST theory.

---

## 1.7 References

- [1] P. Kaur, J.T. Hupp and S.T. Nguyen, *ACS Catalysis*, 1 (2011) 819.
- [2] K. Zhang, B. Tieke, F. Vilela and P.J. Skabara, *Macromolecular Rapid Communications*, 32 (2011) 825.
- [3] R. Dawson, A.I. Cooper and D.J. Adams, *Polymer International*, 62 (2013) 345.
- [4] R.E. Morris and P.S. Wheatley, *Angewandte Chemie International Edition*, 47 (2008) 4966.
- [5] H. Sai, K.W. Tan, K. Hur, E. Asenath-Smith, R. Hovden, Y. Jiang, M. Riccio, D.A. Muller, V. Elser, L.A. Estroff, S.M. Gruner and U. Wiesner, *Science*, 341 (2013) 530.
- [6] J. Hernandez-Montelongo, N. Naveas, S. Degoutin, N. Tabary, F. Chai, V. Spampinato, G. Ceccone, F. Rossi, V. Torres-Costa, M. Manso-Silvan and B. Martel, *Carbohydrate Polymers*, 110 (2014) 238.
- [7] S. Polarz and M. Antonietti, *Chem. Commun.*, (2002) 2593.
- [8] D.A. J. Rouquerol, C. W. Fairbridge, D. H. Everett, J. H. Haynes, and J.D.R. N. Pernicone, K. S. W. Sing and K. K. Unger, *Pure Appl.Chem.*, 66 (1994,) 1739.
- [9] M.A. Carreon, S. Li, J.L. Falconer and R.D. Noble, *J. Am. Chem. Soc.*, 130 (2008) 5412.
- [10] S. Li, J.L. Falconer and R.D. Noble, *Microp. Mesop. Mat.*, 110 (2008) 310.
- [11] D.D. Iarikov and S. Ted Oyama, *Memb. Sci. and Tech.*, 14, Elsevier, (2011), 91.
- [12] Q. Yan, Y. Lin, C. Kong and L. Chen, *Chem. Commun.*, 49 (2013) 6873.
- [13] P. Nugent, Y. Belmabkhout, S.D. Burd, A.J. Cairns, R. Luebke, K. Forrest, T. Pham, S. Ma, B. Space, L. Wojtas, M. Eddaoudi and M.J. Zaworotko, *Nature*, 495 (2013) 80.
- [14] O.K. Farha, I. Eryazici, N.C. Jeong, B.G. Hauser, C.E. Wilmer, A.A. Sarjeant, R.Q. Snurr, S.T. Nguyen, A.Ö. Yazaydin and J.T. Hupp, *J. Am. Chem. Soc.*, 134 (2012) 15016.
- [15] C.F. Martin, E. Stockel, R. Clowes, D.J. Adams, A.I. Cooper, J.J. Pis, F. Rubiera and C. Pevida, *J. Mat. Chemistry*, 21 (2011) 5475.
- [16] P.M. Budd, A. Butler, J. Selbie, K. Mahmood, N.B. McKeown, B. Ghanem, K. Msayib, D. Book and A. Walton, *Phys. Chem. Chem. Phys.*, 9 (2007) 1802.
- [17] H. Furukawa and O.M. Yaghi, *J. Am. Chem. Soc.*, 131 (2009) 8875.
- [18] M.S. Silverstein, *Polymer*, 55 (2014) 304.
- [19] M.S. Silverstein, *Prog. Pol. Sci.*, 39 (2014) 199.
- [20] U. Sevšek, J. Brus, K. Jeřábek and P. Krajnc, *Polymer*, 55 (2014) 410.
- [21] R. Giovannetti., Chapter 6, (2012)
- [22] H. Chen, J. Zeng, F. Deng, X. Luo, Z. Lei and H. Li, *J. Polym. Res.*, 19 (2012) 9880.
- [23] E. Scamporrino and D. Vitalini, *Macromolecules*, 25 (1992) 1625.
- [24] Z. Wang, S. Yuan, A. Mason, B. Reprogle, D.-J. Liu and L. Yu, *Macromolecules*, 45 (2012) 7413.
- [25] L.R.H. High, S.J. Holder and H.V. Penfold, *Macromolecules*, 40 (2007) 7157.
- [26] J.R. Hufton, S. Mayorga and S. Sircar, *AIChE Journal*, 45 (1999) 248.

- [27] Q. Wang, J. Luo, Z. Zhong and A. Borgna, *Environ. Sci.*, 4 (2011) 42.
- [28] H. Yang, Z. Xu, M. Fan, R. Gupta, R.B. Slimane, A.E. Bland and I. Wright, *J. Environ. Sci.*, 20 (2008) 14.
- [29] D.H.Everett and L.K.Koopal, *International union of pure and applied chemistry* (2001).
- [30] N.B. McKeown, S. Hanif, K. Msayib, C.E. Tattershall and P.M. Budd, *Chem. Commun.*, (2002) 2782.
- [31] J. Xia, S. Yuan, Z. Wang, S. Kirklin, B. Dorney, D.-J. Liu and L. Yu, *Macromolecules*, 43 (2010) 3325.
- [32] K.S.W. Sing, D. H.Everett, R.A. W.Haul, L. Moscou, R. A.Pierotti, J. Rouquerol and T. Siemieniewska, *Pure Appl. Chem.*, 57 (1985) 603.
- [33] S. Brunauer, P.H. Emmett and E. Teller, *J. Am. Chem. Soc.*, 60 (1938) 309.
- [34] F. Rouquerol, J. Rouquerol and K. Sing, *Academic press*, (1999).
- [35] H. Marsh and B. Rand, *J. Col. Int. Sci.*, 33 (1970) 101.
- [36] F. Carrasco-Marin, M.V. Lopez-Ramon and C. Moreno-Castilla, *Langmuir*, 9 (1993) 2758.
- [37] C. Nguyen and D.D. Do, *Carbon*, 39 (2001) 1327.
- [38] C. Lastoskie, K.E. Gubbins and N. Quirke, *J. Phys. Chem.*, 97 (1993) 4786.
- [39] J.P. Olivier, W.B. Conklin and M.v. Szombathely, in F.R.-R.K.S.W.S. J. Rouquerol and K.K. Unger (Editors), *Studies in Surface Science and Catalysis*, 87, Elsevier, (1994), 81.
- [40] J. Landers, G.Y. Gor and A.V. Neimark, *Col. Surf. A: Physicochem. Eng. Aspects* (2013) 3.
- [41] L. Czepirski and J. Jagiełło, *Chem. Eng. Sci.*, 44 (1989) 797.
- [42] W.V. Smith, *J. Am. Chem. Soc.*, 70 (1948) 3695.
- [43] W.V. Smith and R.H. Ewart, *J. Chem.Phys.*, 16 (1948) 592.
- [44] J. Qiu, B. Charleux and K. Matyjaszewski, *Progr. Pol. Sci.*, 26 (2001) 2083.
- [45] G. Odian, 4th Edition (2004).
- [46] C.D. Anderson and E.S. Daniels, *Rapra Review Reports*, 14 ( 2003).

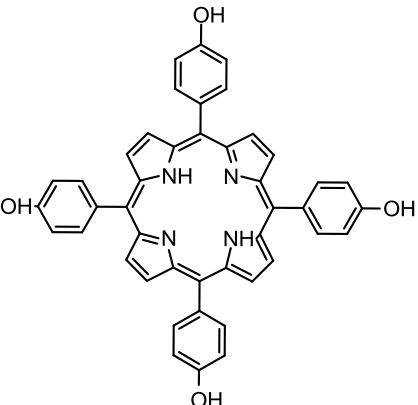
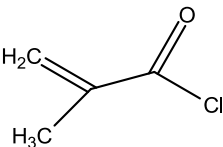
## 2 Experimental

### 2.1 Experimental process

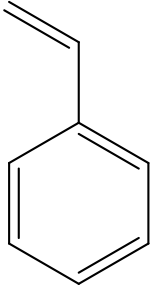
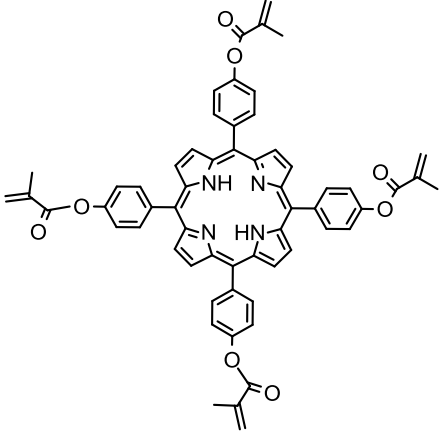
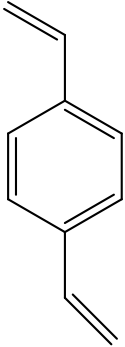
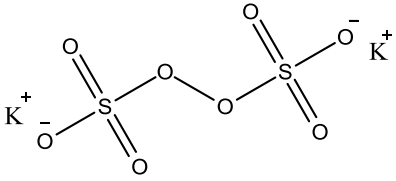
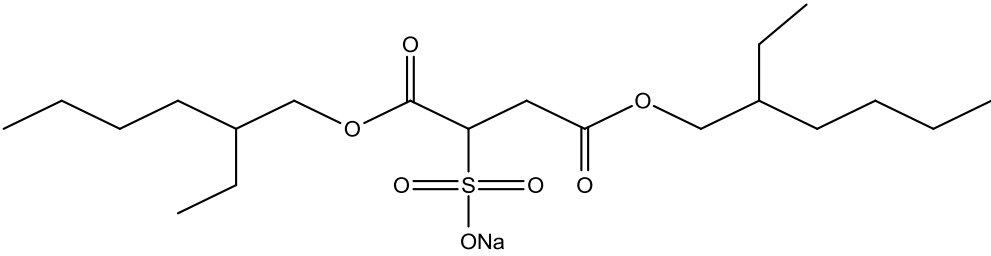
#### 2.1.1 Materials

5, 10, 15, 20-Tetrakis (4-hydroxyphenyl)-21H, 23H-porphine (95%), methacryloyl chloride (97%, Fluka), styrene (99%) and divinylbenzene (technical grade, 80%) were purchased from Sigma-Aldrich. Dioctyl sulfosuccinate, sodium salt (98%) was used as the surfactant and was purchased from Sigma-Aldrich. In addition, potassium peroxydisulfate (99%) was used as the initiator and was obtained from Riedel-de Haën. Ethanol (absolute, 98%) was obtained from Sigma-Aldrich and N, N-Dimethylformamide (extra pure, 99.9%), toluene (analytical grade, 99.6%), triethylamine (synthesis grade, 99%), and tetrahydrofuran (HPLC grade, 99.9%) were purchased from Scharlau. Milli-Q water was used in all experiments. The tables below depict the chemical structures of the main chemicals used for porphyrin functionalization and the cross-linkers, surfactant and initiator used for the porous particles synthesis.

**Table 2.1** Chemical structures of the chemicals used for porphyrin functionalization.

 <p>5, 10, 15, 20-Tetrakis (4-hydroxyphenyl)- 21H, 23H-porphine</p>	 <p>MCl methacryloyl chloride</p>
--	---

**Table 2.2** Chemical structures of the monomers, cross-linkers, surfactant and initiator used for the porous particles synthesis.

 <p style="text-align: center;">St styrene</p>	 <p style="text-align: center;">PO tetra-vinyl functionalized porphyrin</p>
 <p style="text-align: center;">DVB divinylbenzene</p>	 <p style="text-align: center;">KPS potassium persulfate</p>
 <p style="text-align: center;">AOT dioctyl sulfosuccinate, sodium salt</p>	

### 2.1.2 Polystyrene particles

The synthesis of the polystyrene particles was carried out by a typical emulsion free-radical copolymerization of styrene and a bifunctional cross-linker, divinylbenzene, in the presence of a surfactant, AOT. The synthetic process of the microgel particles is described below in detail. The polymerization took place in a 25ml round bottom flask containing 5 wt% water (with respect to monomer) and 1-10 wt% AOT to monomer. Next, styrene (St) (0.6gr) and divinylbenzene (DVB) (0.006gr) was added under continuous stirring. The reaction was then degassed for 30 minutes. Finally, the flask was placed in a thermostatted oil bath at 60°C under stirring for one hour before the addition of 1 wt%  $K_2S_2O_8$  (with respect to the monomer) which initiated the polymerization process. The reaction was allowed to proceed overnight before cooling under water and was exposed to air to quench the polymerization. The final polymer particles were purified using dialysis (molecular weight cut-off of the membrane: 3500 dalton) to remove any unreacted materials. The purification process continued for one week and the water was exchanged twice a day.

The same process was carried out for the synthesis of the hyper-cross-linked polystyrene particles by adding styrene (St) (0.6gr) and divinylbenzene (DVB) (1.11gr) with a mole ratio of 40 to 60.

### 2.1.3 Porphyrin functionalization reaction

The tetra-methacrylate functionalized porphyrin was obtained via an esterification reaction of 5, 10, 15, 20-Tetrakis (4-hydroxyphenyl)-21H, 23H-porphine with methacryloyl chloride. The process took place in a 100ml round bottom flask containing the porphyrin (0.40 gr) which was previously dried under vacuum overnight. Next, 30 ml dry THF were added in the flask under stirring until the porphyrin was dissolved. After that, 2 ml distilled TEA was added and the flask was placed in an ice bath before the addition of 0.22 ml distilled MCl and another 10 ml dry THF. The reaction was purged with  $N_2$  for one minute and was allowed to proceed for three days at room temperature. Then the mixture was filtered under  $N_2$ , to remove the TEA salt formed and any unreacted porphyrin, into a 250 ml round bottom flask and then distilled to obtain the solid functionalized porphyrin and assess the purity of the product  $H^1$ -NMR spectroscopy was used. If necessary the product

was further purified by passing through an alumina packed column using a dichloromethane and ethanol 99-1 v/v % solvent mixture.

#### **2.1.4 Synthesis of porphyrin-containing particles**

The synthesis of the crosslinked particles was carried out by emulsion free-radical copolymerization of styrene, using the tetra-methacrylate functionalized porphyrin and DVB as the crosslinkers in the presence of AOT as the surfactant. The synthesis described below is a typical process followed for the microgel particle preparation. The polymerization took place in a 25 ml round bottom flask containing 5 wt % water and 5 wt % AOT (with respect to PO-S-D). Next, a mixture of styrene (St) (0.205gr), functionalized porphyrin (PO) (0.04 gr) and divinylbenzene (DVB) (0.37 gr) was added under continuous stirring. The minimum possible amount of toluene was used for some samples as a co-solvent of the PO. The reaction was then degassed for 20 minutes and sonicated for one hour until complete dispersion of the monomers. Finally, the flask was placed in a thermostatted oil bath at 60°C under intense stirring and the reaction was allowed to proceed overnight before cooling under water and was exposed to air to quench the polymerization. The final polymer particles were purified using dialysis (molecular weight cut-off of the membrane: 3500 dalton) to remove any unreacted materials. The purification process continued for one week and the water was exchanged twice a day. The crosslink density of the polymer particles was varied by increasing progressively the PO content from 0.9 to 12 mole % with respect to DVB at a constant St:cross-linker (PO and DVB) mole ratio of 40/60.

## **2.2 Sample preparation**

### **2.2.1 Scanning Electron Microscopy (SEM)**

Scanning electron micrographs were recorded using a field-emission JEOL 7000 electron microscope operating at 10 kV. Samples were prepared by diluting the particle dispersion in water and depositing a drop of the dispersion onto a silicon or glass slide and allowing it to dry in air overnight. The slides were then sputter-coated with a 10 nm Au film to reduce charging during the measurements.



### **2.2.2 Transmission Electron Microscopy (TEM)**

A JEOL JEM-2100 instrument at an electron accelerating voltage of 80 kV was used for the measurements. TEM samples were prepared following the same process as that described above for the SEM samples. A drop of the sample was placed on a carbon grid and was allowed to dry in air overnight.

### **2.2.3 Dynamic Light Scattering (DLS)**

A 3DDLS Spectrometer from LS Instruments with a HeNe laser operating at  $\lambda=632.8$  nm was used for all the measurements which were performed at 20°C. The samples were measured for 200 seconds at each scattering angle. All samples were filtered through a 0.45  $\mu\text{m}$  pore size syringe filter and were sonicated before the measurement.

### **2.2.4 Ultraviolet/ Visible Spectroscopy (UV/Vis)**

A Lambda 25 UV/VIS spectrometer from Perkin Elmer was used for the measurements. The samples were diluted with an appropriate solvent to obtain 10ml of sample at the desirable concentration. For the measurement the samples were transferred to a 10 mm quartz cuvette.

### **2.2.5 Nuclear Magnetic Resonance (NMR)**

A 300MHz Bruker  $^1\text{H}$  NMR spectrometer was used for the measurements. The samples were dissolved in deuterated chloroform (Chloroform-d) and were then transferred to an NMR tube in order to perform the measurements.

### **2.2.6 Supercritical Point Drying (SPD)**

A Bal-Tec CPD 030 critical point dryer was used for carrying out the drying process. The drying procedure followed involved first the exchange of the solvent from water to ethanol (through THF) or dimethylformamide using a dialysis membrane. After that the remaining solvent in the pores was effectively removed by

supercritical drying with CO<sub>2</sub> at 10°C over a period of 10 hours to obtain open-pore polymer structures.

### **2.2.7 Gas adsorption Isotherms**

Gas adsorption experiments in this study were conducted using a Quantachrome Model NOVA 3200e Gas Sorption Analyzer. Nitrogen and carbon dioxide gas were selected as the adsorbates. The gas adsorption data were analyzed using the multipoint BET and the DR gas adsorption theories in order to determine the surface area of the samples. The non-local Density Functional Theory (NLDFT) method was employed to determine the pore size distribution and the pore volume of the samples. Before the measurement the samples were outgassed at 80 °C under vacuum for 12 h. The N<sub>2</sub> isotherms were obtained using a liquid nitrogen bath (at 77 K) while, the CO<sub>2</sub> isotherms were obtained at 273 K.

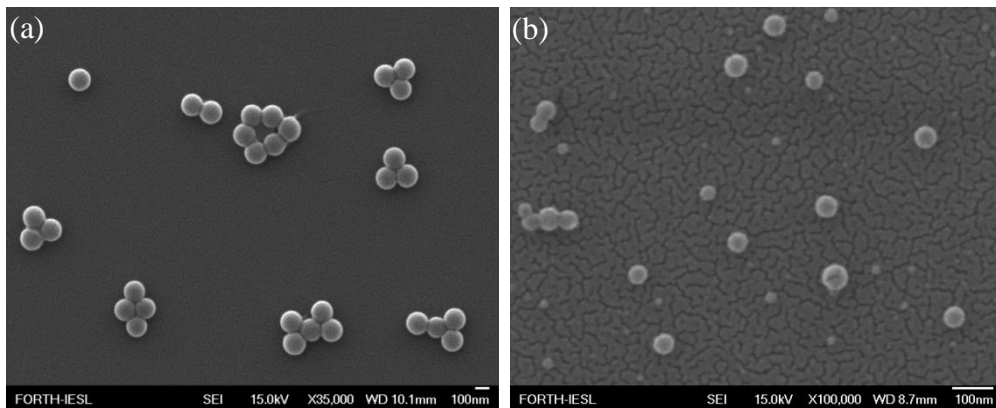
## 3 Results and Discussion

### 3.1 Synthesis of cross-linked polystyrene nanoparticles

In order to successfully synthesize monodisperse cross-linked polystyrene nanoparticles stabilized with AOT a number of syntheses were carried via emulsion polymerization while altering the percentage of stabilizer used in each case. After synthesis, the nanoparticles were observed by SEM to investigate the particles' morphology, size and polydispersity.

#### 3.1.1 Polystyrene nanoparticles using different percentage of AOT

Four samples of lightly cross-linked colloidal PS nanoparticles were prepared via a typical emulsion copolymerization process of styrene (St) and divinylbenzene (DVB), while changing the weight fraction of AOT from 1-10 % with respect to the monomer and cross-linker. The particles were characterized by SEM. Figures 3.1 a-d show characteristic images of the samples prepared. In all cases spherical particles were observed. The sample with 1 % AOT exhibited the lowest polydispersity with a mean particle diameter of  $162 \pm 5$  nm while the rest of the samples exhibited a decrease in the particle size and an increase in polydispersity with the amount of stabilizer used (**Figure 3.2**). The average particle sizes and polydispersities are summarized in **Table 3.1**.



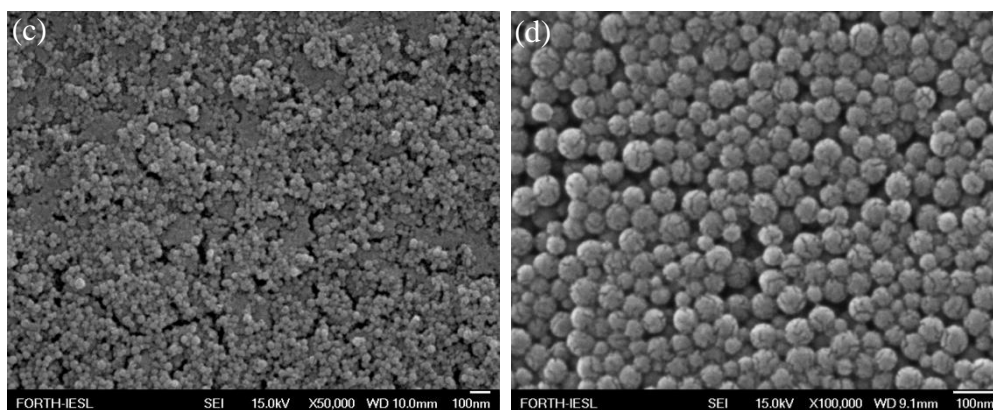


**Figure 3.1** SEM images of cross-linked polystyrene nanoparticles prepared using (a) 1% AOT, (b) 3% AOT, (c) 8% AOT and (d) 10% AOT.

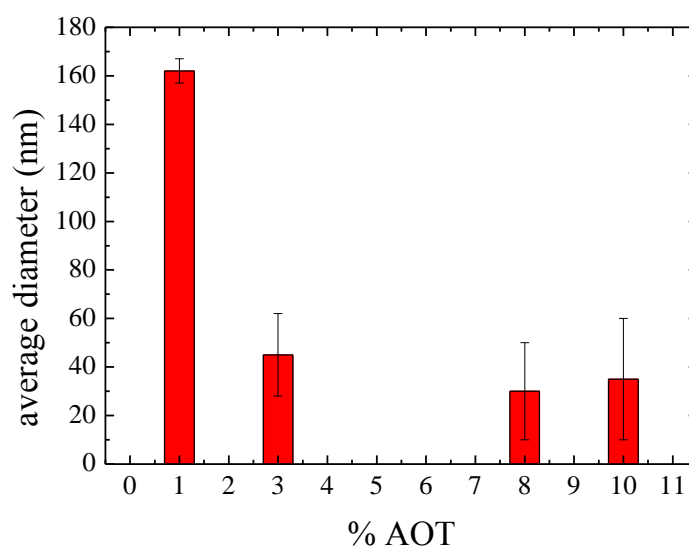


**Figure 3.2** Average particle diameter as a function of the fraction of AOT used upon synthesis.

**Table 3.1** Sample characteristics and particle sizes by SEM and DLS for the lightly cross-linked polystyrene particles.

Sample	% AOT	St:DVB mole ratio	Mean particle diameter (by SEM)	R <sub>h</sub> by DLS
PS-1%	1	99.17:0.83	162 ± 5 nm	81 nm
PS-3%	3	99.17:0.83	45 ± 17 nm	-
PS-8%	8	99.17:0.83	30 ± 20 nm	-
PS-10%	10	99.17:0.83	35 ± 25 nm	-

Sample PS-1% was quite monodisperse, as seen from the SEM images and the table above, thus it was further investigated using DLS measurements in water to determine the hydrodynamic size of the polystyrene particles. The single exponential decay of the autocorrelation functions and the linear increase of the decay rates confirmed the monodisperse particle size (**Figure 3.3**). The diffusion coefficient of the single exponential process was found to be  $D = 2.64 \cdot 10^{-12} \text{ m}^2/\text{s}$  which corresponds to a hydrodynamic radius of 81 nm (162 nm particle diameter).

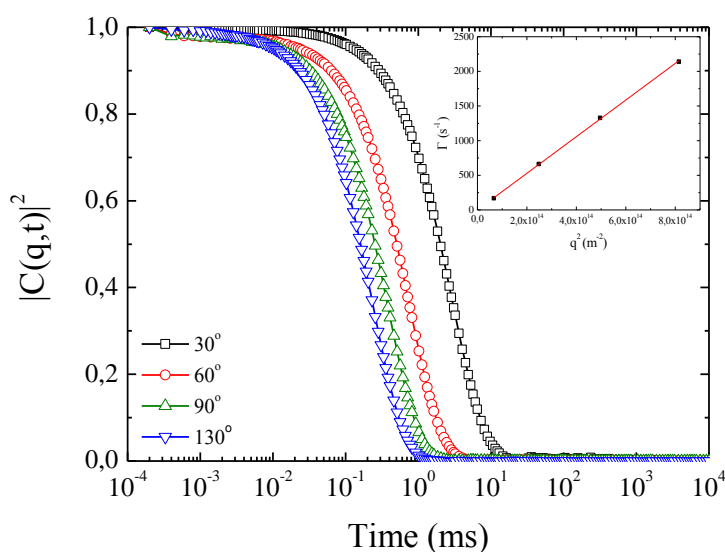


**Figure 3.3** Intensity autocorrelation functions of the PS-1% sample in water at different scattering angles. Inset: Decay rate ( $\Gamma$ ) as a function of the square of the wavevector ( $q^2$ ).

Moreover, the DLS measurements confirmed that the PS-1% sample was well stabilized in water since no aggregates were found.

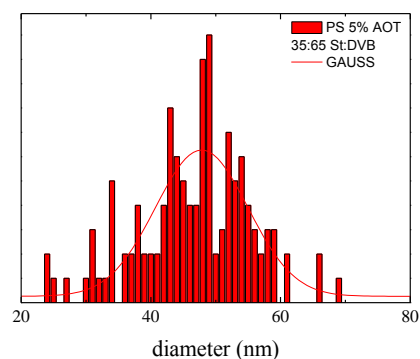
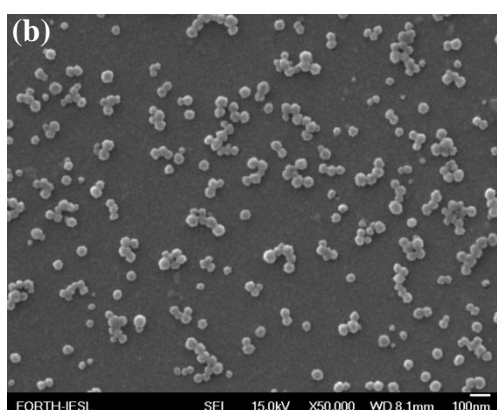
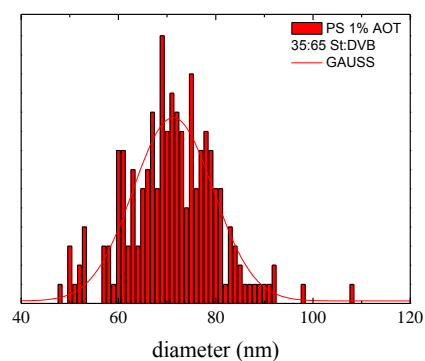
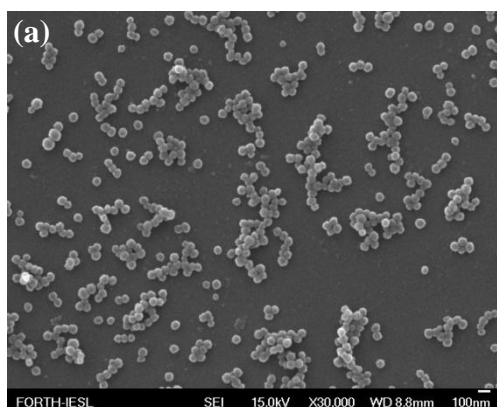
### 3.2 Highly cross-linked polystyrene particles

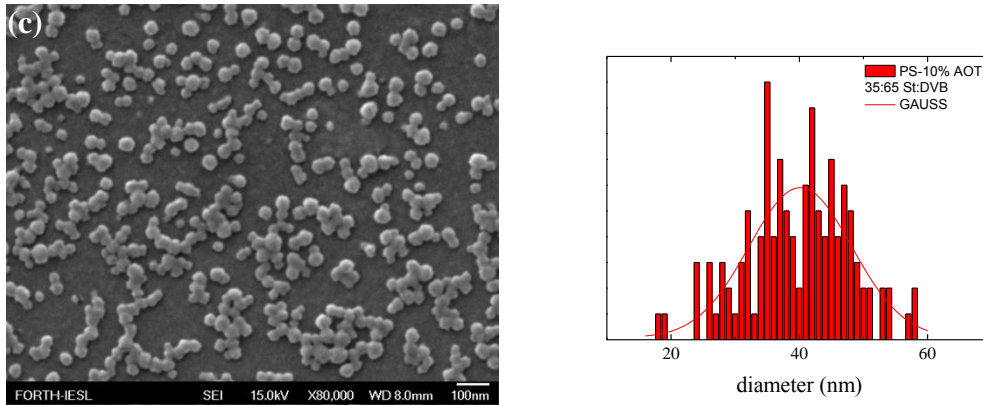
Following the preparation of the monodisperse colloidal PS particles we proceeded with the synthesis of a series of highly cross-linked polystyrene particles. The particles were prepared via emulsion copolymerization by altering the percentage of AOT stabilizer while the mole ratio of St to DVB was kept constant at 40:60. After

synthesis the PS particles were characterized by SEM in order to investigate the particles morphology, size and polydispersity.

### 3.2.1 Highly cross-linked polystyrene nanoparticles using different percentage of AOT

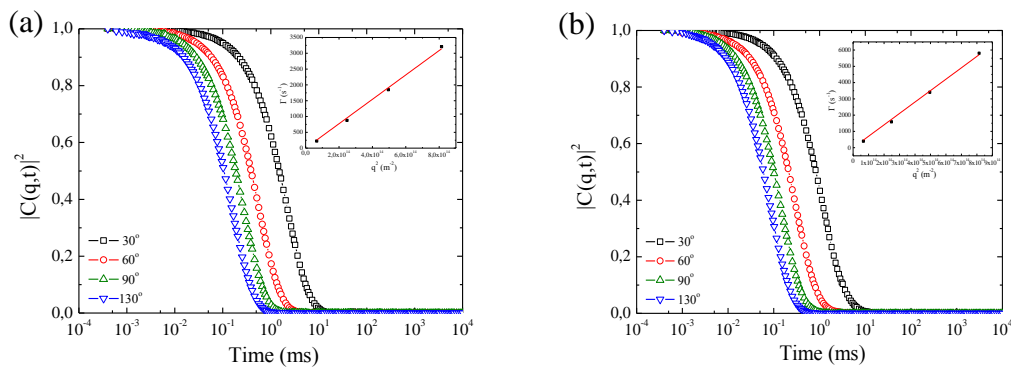
Three samples were prepared via a typical emulsion copolymerization process of St using DVB as the crosslinker, at a constant 40:60 mole ratio, and while altering the AOT weight fraction with respect to the monomer and cross-linker from 1- 10 %. The effect of AOT on the particle size, size uniformity and stabilization was assessed. The particles were examined by SEM and characteristic images are shown in **Figures 3.4(a-c)**. For all samples spherical particles were observed. The sample with 1 wt % AOT showed larger particles in comparison with that containing 5 wt % and 10 wt % AOT.





**Figure 3.4** SEM images and the corresponding particle size distributions for samples with a 40:60 mole ratio St:DVB and (a) 1% AOT, (b) 5% AOT and (c) 10% AOT.

The samples were further investigated by DLS measurements in water in order to determine the hydrodynamic size of the highly cross-linked polystyrene particles. The single exponential decay of the autocorrelation functions and the linear increase of the decay rates confirmed the particles monodispersity and uniform size (**Figure 3.5**). For sample PS-1% 40:60 St:DVB the diffusion coefficient of the single exponential process was found to be  $D = 3.85 \cdot 10^{-12} \text{ m}^2/\text{s}$ , which corresponds to a hydrodynamic radius of 56 nm (112 nm particle diameter). For sample PS-5% 40:60 St:DVB the diffusion coefficient of the single exponential process was found to be  $D = 7.01 \cdot 10^{-12} \text{ m}^2/\text{s}$  which corresponds to a hydrodynamic radius of 31 nm (62 nm particle diameter) whereas, for sample PS-10% 40:60 St:DVB the diffusion coefficient of the single exponential process was found to be  $D = 6.38 \cdot 10^{-12} \text{ m}^2/\text{s}$  which corresponds to a hydrodynamic radius of 34 nm (68 nm particle diameter).



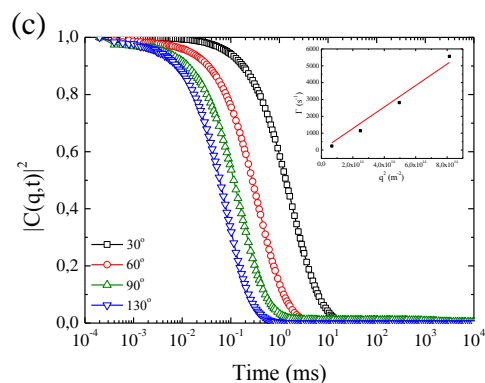


**Figure 3.5** Intensity autocorrelation functions of the samples (a) PS-1% 40:60 St:DVB, (b) PS-5% 40:60 St:DVB and (c) PS-10% 40:60 St:DVB in water at different scattering angles. Inset: Decay rate of the autocorrelation functions ( $\Gamma$ ) as a function of the square of the wavevector ( $q^2$ ).

The above results are summarized in **Table 3.2** and are compared to sizes of the lightly cross-linked polystyrene samples. Samples with 1 and 5 wt % AOT appeared to be more stable in water, whereas the PS-1% 40:60 St:DVB sample had the larger particle diameter as expected, and this synthetic protocol was followed for the synthesis of porphyrin containing particles.

Moreover, it is noted that as the cross-link density increases for the same AOT content, sample PS-1% and sample PS-1% 40:60 St:DVB, the particles hydrodynamic diameter decreases from 162 nm (see Table 3.1) to 112 nm, respectively.

**Table 3.2** sample characteristics and particle sizes for the highly cross-linked polystyrene particles.

Sample	wt % AOT with respect to St and DVB	St:DVB mole ratio	Mean particle diameter (by SEM)	$R_h$ by DLS
<b>PS-1% 40:60 St:DVB</b>	1	40:60	$71 \pm 16$ nm	56 nm
<b>PS-5% 40:60 St:DVB</b>	5	40:60	$48 \pm 14$ nm	31 nm
<b>PS-10% 40:60 St:DVB</b>	10	40:60	$40 \pm 16$ nm	34 nm



### 3.3 Porphyrin functionalization reaction

An esterification reaction was carried out for the functionalization of the porphyrin molecule to a tetra-methacrylate analogue, using methacryloyl chloride as described in Section 2.1.4. Triethylamine was used to bind the HCl formed during the esterification reaction and precipitated as a salt in the organic reaction medium thus pushing the reaction to quantitative yield (**Figure 3.6**).

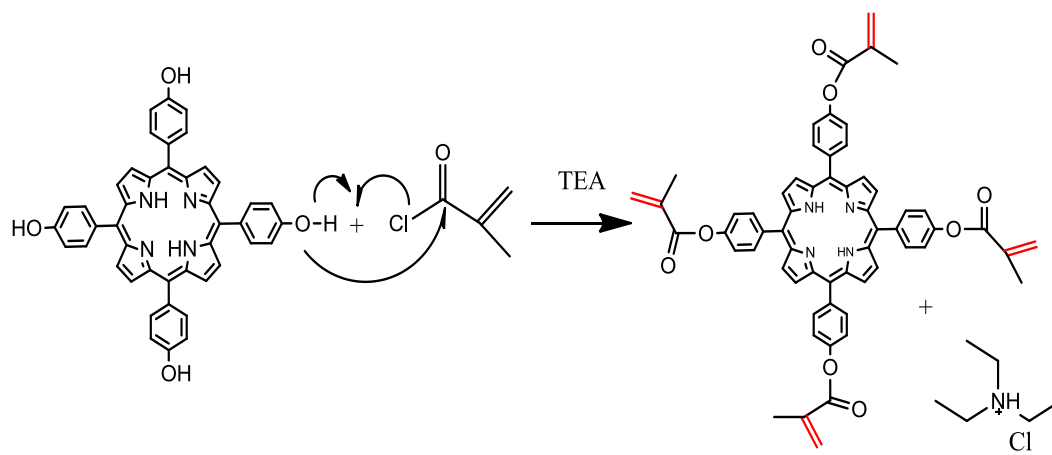


**Figure 3.6** Schematic representation of the tetra-hydroxy porphyrin functionalization reaction.

The successful functionalization of the tetra-hydroxy porphyrin molecule was confirmed using  $^1\text{H-NMR}$  spectroscopy (**Figure 3.7**). The peak at -2.82 ppm corresponds to the two protons of the porphyrin macrocycle which are highly protected. The peak at 8.90 ppm corresponds to the 8 protons of the porphyrin macrocycle. The peaks at 7.54 and 8.22 ppm correspond to the protons of the four phenyl groups of the porphyrin. The peak at 2.23 ppm corresponds to the twelve protons of the methyl groups of the incorporated methacrylate moieties, whereas the peaks at 5.91 and 6.56 ppm correspond to the protons of the methylene group of the methacrylate groups. The above assigned peaks and the lack of any additional peaks verify the successful synthesis and the purity of the synthesized functional polymerizable porphyrin molecules.

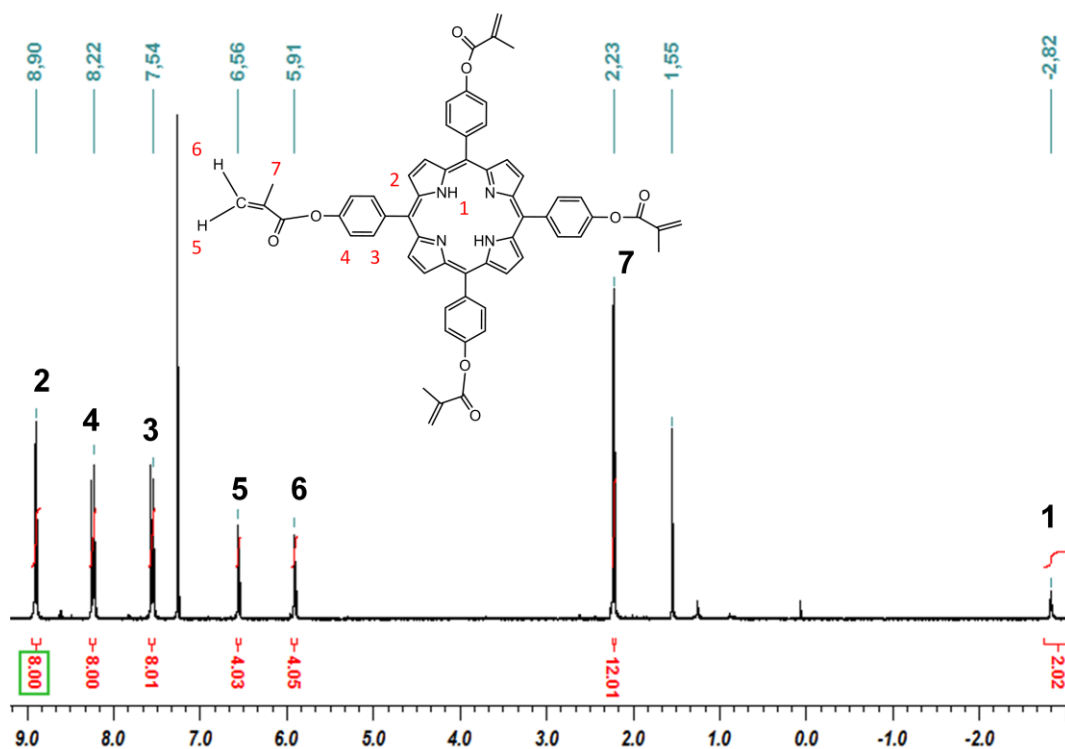


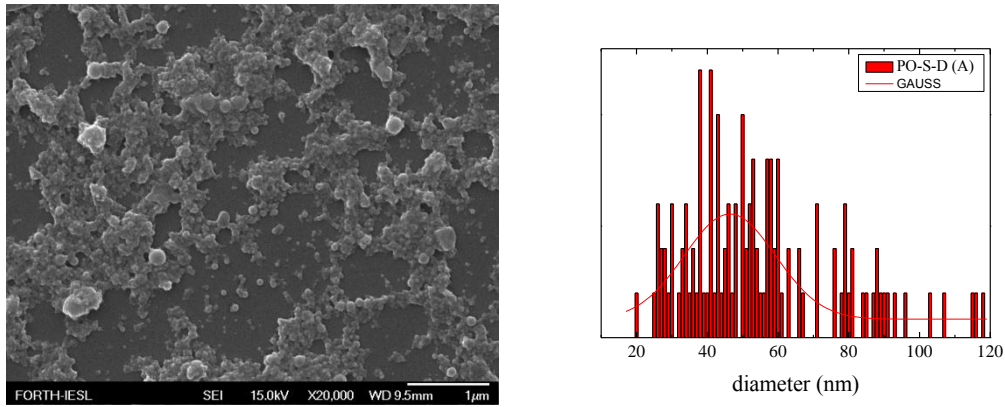
**Figure 3.7**  $^1\text{H-NMR}$  spectrum of the tetra-methacrylate functionalized porphyrin molecule in  $\text{CDCl}_3$ .

### 3.4 Porphyrin containing highly cross-linked polystyrene nanoparticles

Based on the results summarized in **Table 3.2** porphyrin containing colloidal particles were synthesized as described in Section 2.1.5. Samples with 1 wt % AOT with respect to the monomers and a 40:60 mole ratio of styrene (St) with respect to the cross-linker (both porphyrin and DVB) were prepared and characterized.

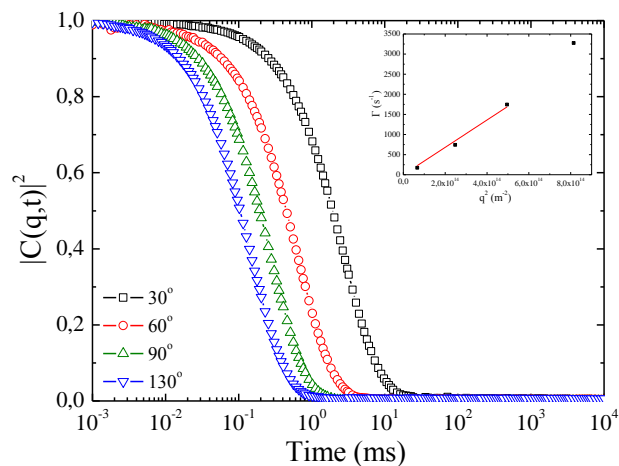
#### 3.4.1 Porphyrin containing particles with 1 wt % AOT

First, a sample with 1 wt % AOT was synthesized leading to unstable particles that coagulated (sample PO-S-D (A)) in water. The particles size as observed by SEM was found to be  $46 \pm 26$  nm (**Figure 3.8**).



**Figure 3.8** SEM image and corresponding particle diameter size distribution for sample PO-S-D(A) 1 wt % AOT.

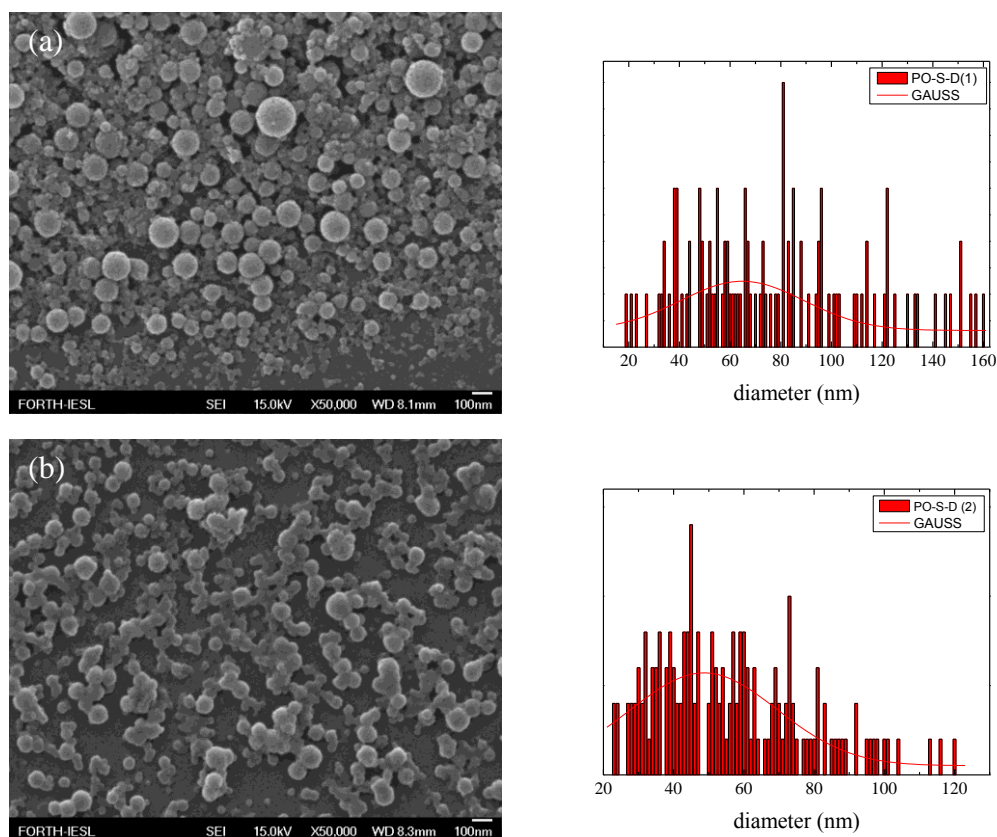
The sample PO-S-D (A) was further investigated by DLS measurements in water to determine the hydrodynamic size of the particles after filtration with a 0.45 nm pore size filter. The single exponential decay of the autocorrelation functions and the linear increase of the decay rate (**Figure 3.9**) were attributed to a single particle population. The diffusion coefficient of the single process was found to be  $D = 3.40 \cdot 10^{-12} \text{ m}^2/\text{s}$  which corresponds to a hydrodynamic radius of 63 nm (126 nm diameter).

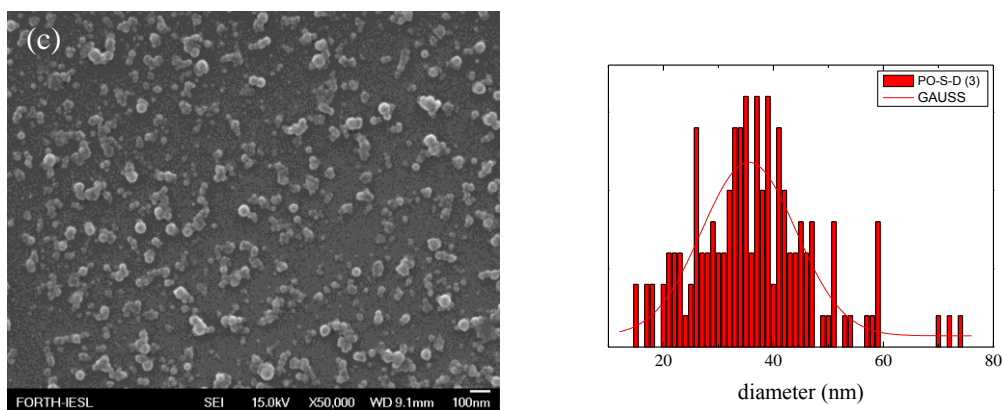


**Figure 3.9** Intensity autocorrelation functions of the sample PO-S-D (A) 1 wt % AOT in water at different scattering angles. Inset: Decay rate of the autocorrelation functions ( $\Gamma$ ) as a function of the square of the wavevector ( $q^2$ ).

### 3.4.2 Porphyrin containing particles with 5 wt % AOT

Based on the above results and in order to solve the stabilization problem of the polystyrene particles, a series of samples were prepared by a typical emulsion copolymerization process of styrene, divinylbenzene and porphyrin using 5 wt % AOT with respect to the monomers. In all cases the mole ratio of styrene to the cross-linkers was kept constant at 40:60 while altering the porphyrin content from 0.9 to 12 mole %. The first sample PO-S-D (1) had a 0.9 mole % porphyrin, the second sample PO-S-D (2) 3.5 mole % porphyrin whereas the third sample PO-S-D (3) contained a significantly higher porphyrin content 12 mole % with respect to the total monomer and cross-linkers used. It is noted that for samples PO-S-D (2) and PO-S-D (3) toluene was used as a co-solvent to efficiently dissolve the PO in the reaction mixture. After synthesis the samples were observed by SEM and characteristic images are shown in **Figure 3.10**. In all cases spherical particles with a high polydispersity were observed which suggested that the incorporation of the PO limited the control of the emulsion polymerization process.

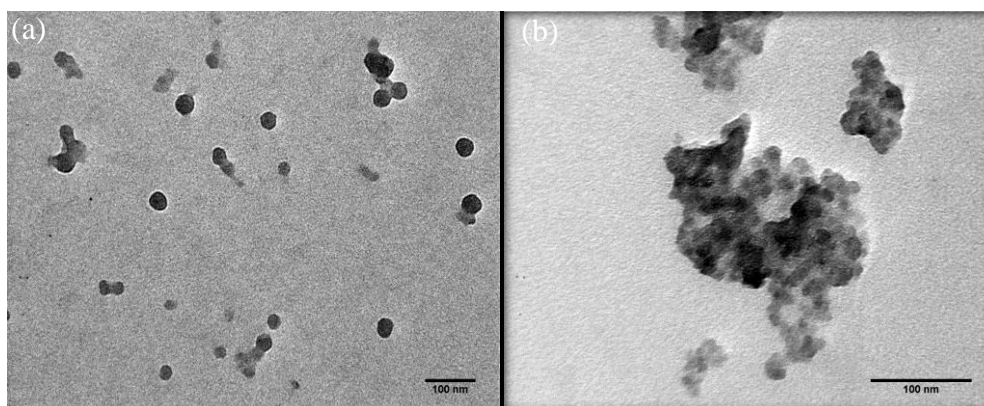


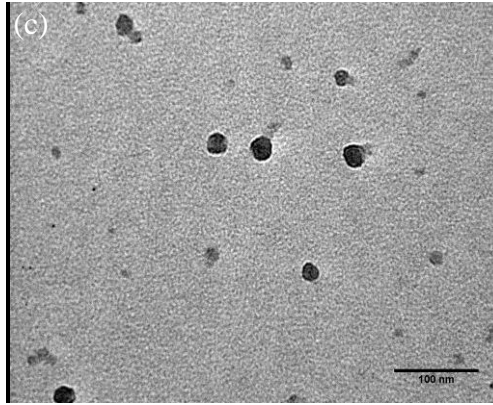


**Figure 3.10** SEM images and corresponding particle diameter size distribution for samples (a) PO-S-D (1), (b) PO-S-D (2) and (c) PO-S-D (3).

The mean particles size was found to decrease as the cross-link density of the particles increased from 64 nm for PO-S-D (1) to 49 nm for PO-S-D (2) and 36 nm for PO-S-D (3). On the other hand, both samples PO-S-D (1) and PO-S-D (2) appeared to be highly polydisperse with a particle size distribution of  $64 \pm 48$  nm and  $49 \pm 42$  nm, respectively, whereas sample PO-S-D (3) was slightly less polydisperse,  $36 \pm 17$  nm, which was attributed to the larger amount of toluene used upon synthesis of the particles.

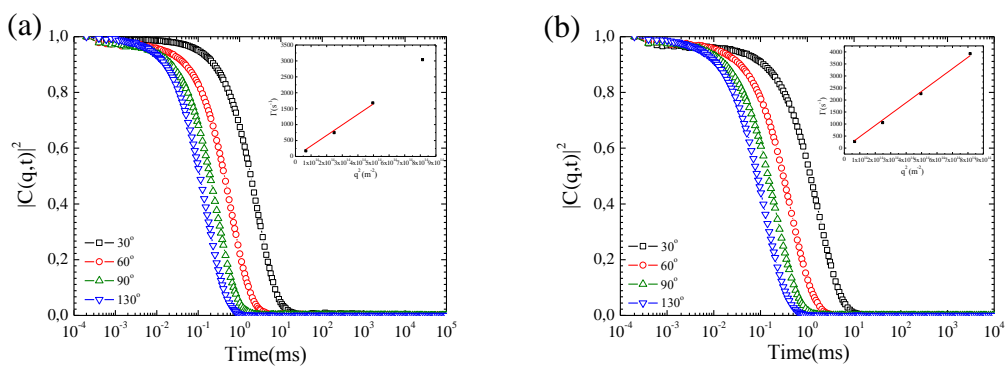
The samples were further analyzed by TEM (see **Figure 3.11**). The darker color which provided contrast to the polymeric particles was attributed to the presence of aromatic moieties in the particles (St, DVB and porphyrin). The size of the particles was estimated to be the same as that found by SEM.





**Figure 3.11** TEM images for samples (a) PO-S-D (1), (b) PO-S-D (2) and (c) PO-S-D (3) prepared with the dipping technique.

Next, and despite the polydispersity of the samples the particles were further investigated with DLS measurements in water in order to determine the hydrodynamic size of the particles. The single exponential decay of the autocorrelation functions and the linear increase of the decay rate were analyzed (**Figure 3.12**). The diffusion coefficients for samples PO-S-D (1), PO-S-D (2) and PO-S-D (3) were found to be  $D = 3.31 \cdot 10^{-12} \text{ m}^2/\text{s}$ ,  $D = 4.72 \cdot 10^{-12} \text{ m}^2/\text{s}$  and  $D = 5.99 \cdot 10^{-12} \text{ m}^2/\text{s}$  which correspond to hydrodynamic radii of 65 nm (130 nm diameter), 45 nm (90 nm diameter) and 36 nm (72 nm diameter), respectively. These results verify the decrease of the mean particles size when increasing the cross-link density of the particles, which was also found by SEM.



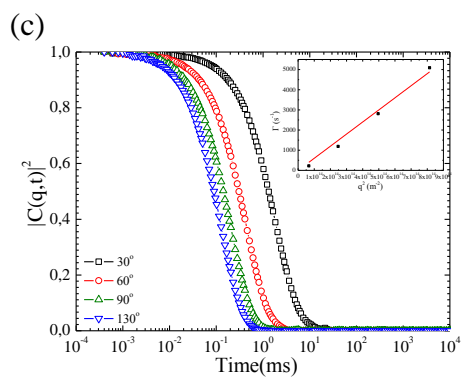


**Figure 3.12** Intensity autocorrelation functions of the samples (a) PO-S-D (1), (b) PO-S-D (2) and (c) PO-S-D (3) in water at different scattering angles. Inset: Decay rates of the autocorrelation functions ( $\Gamma$ ) as a function of the square of the wavevector ( $q^2$ ).

All the above results are summarized for a better comparison in **Table 3.3**

**Table 3.3** Comparison table of the porphyrin containing particles with 5% AOT

Sample	PO-St-DVB mole ratio	$D_{av.}$ by SEM	$D_{av.}$ by TEM	$R_h$ by DLS
PO-S-D (1)	0.9-40-59.1	$64 \pm 48$ nm	20-130 nm	65 nm
PO-S-D (2)	3.5-40-56.5	$49 \pm 42$ nm	15-60 nm	45 nm
PO-S-D (3)	12-40-48	$36 \pm 17$ nm	10-40 nm	36 nm



### 3.4.3 Porphyrin content of the particles with 5 wt % AOT

Next, UV/Vis measurements were employed in order to verify the presence of the porphyrin moieties within the synthesized colloidal particles and determine the porphyrin content of the samples. For the analysis, first a calibration curve was constructed in order to correlate the absorption intensity with the concentration of the porphyrin in solution.

#### 3.4.3.1 Calibration curve of porphyrin solutions

The tetra-methacrylate functionalized porphyrin has a specific UV/Vis spectrum with a major peak at 418 nm which corresponds to the near-UV Soret band of the porphyrin and four peaks of lower intensity at 514 nm, 548 nm, 592 nm and 648 nm which correspond to the Q-bands (**Figure 3.13**).

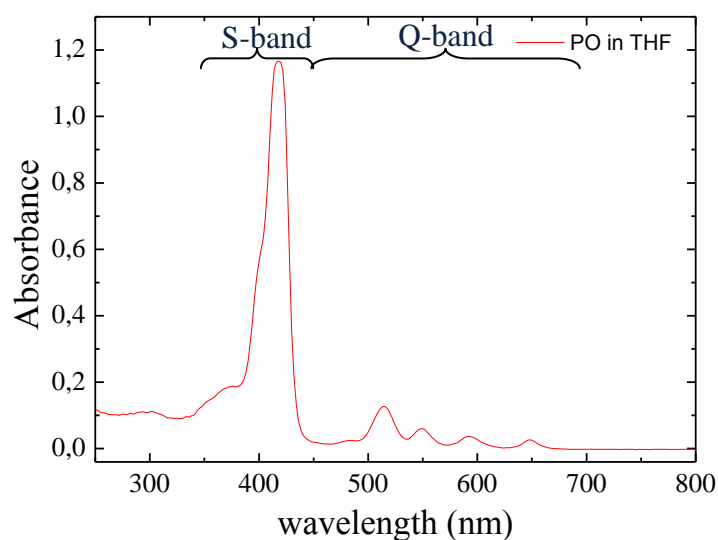


**Figure 3.13** UV/Vis spectrum of the tetra-methacrylate functionalized porphyrin in THF

Samples were prepared using the tetra-methacrylate functionalized porphyrin diluted in THF at different concentrations. Four samples were prepared in total with concentrations ranging from  $1.1 \cdot 10^{-5}$  mol/L up to  $4.125 \cdot 10^{-5}$  mol/L (**Figure 3.14**) and the measurements were performed in a 1 cm quartz cuvette.



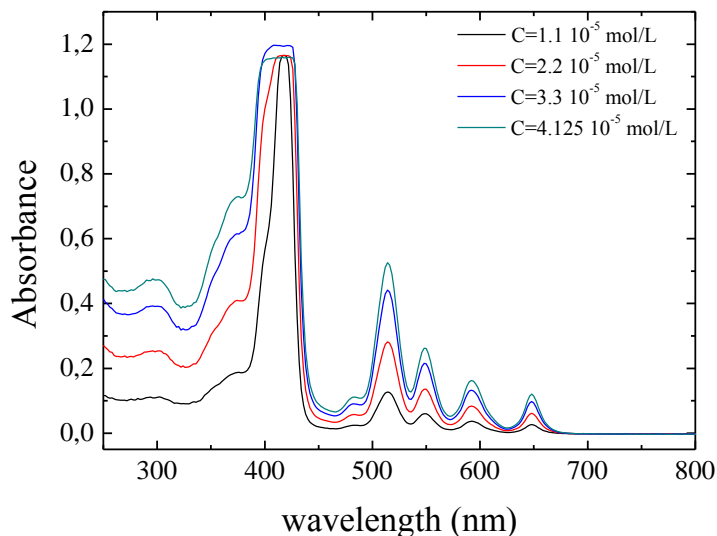


**Figure 3.14** UV/Vis spectra of the four porphyrin samples in THF with concentrations in the range of  $1.1 \cdot 10^{-5}$  to  $4.125 \cdot 10^{-5}$  mol/L

For the calibration curve the major S-band at 418 nm could not be used due to saturation of the intensity at the higher concentrations. It is also noted that the absorption spectra of the polymer particles exhibited an increase of the intensity in the visible region due to the scattering by the particles and thus the peak at 648 nm was used for the calibration curve which is at the longer wavelength. Based on the Beer-Lambert law  $A = \epsilon b c$ , and using the absorption intensity as a function of porphyrin concentration (mol/L) (**Figure 3.14**) a plot of  $A$  versus  $c$  was constructed (**Figure 3.15**) the linear fit of which corresponds to the molecular absorption coefficient ( $\epsilon$ ) multiplied with the size of the cuvette ( $b$ ), which in this case is 1 cm. From this linear fit  $\epsilon b$  was calculated to be  $3113 \text{ M}^{-1}$ .

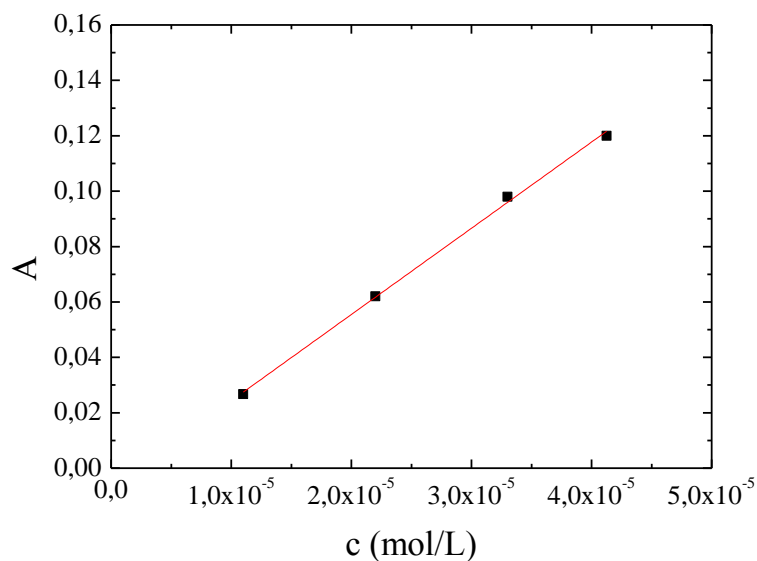


**Figure 3.15** Calibration curve of the absorption intensity versus the porphyrin concentration.

### 3.4.3.2 UV/Vis characterization of the porphyrin containing colloidal particles

In order to determine the porphyrin content of the colloidal particles samples PO-S-D (1), PO-S-D (2) and PO-S-D (3) were first diluted in THF. The theoretical content of the porphyrin for all three samples was calculated from the mass of PO, St and DVB used for each reaction during synthesis and the results are presented in **Table 3.4**. Next, the polymer particles dispersed in THF were measured by UV/Vis spectroscopy and the spectra were analyzed using the band at 648 nm (the same band was used for the construction of the calibration curve described above). For sample PO-S-D (1) the particle concentration in THF was  $6.25 \cdot 10^{-5}$  gr/ml and the experimental porphyrin content was calculated at 4.8 wt % which is in relative good agreement with the theoretical value of 6.2 wt %. For sample PO-S-D (2) the particle concentration in THF was  $3.69 \cdot 10^{-5}$  gr/ml and the experimental porphyrin content was calculated at 16.2 wt % which is lower than the theoretical content of 22.1 wt %. Finally, for sample PO-S-D (3) the sample concentration in THF was  $1.56 \cdot 10^{-5}$  gr/ml. However, the spectrum was similar to that of the tetra-methacrylate porphyrin with no obvious polystyrene peak at  $\sim 260$ nm, suggesting the absence of polymer within the particles (**Figure 3.16**). Thus, no experimental porphyrin content was calculated.

Porphyrin appeared to destabilize the emulsion polymerization process since solid polystyrene precipitated during the reaction.

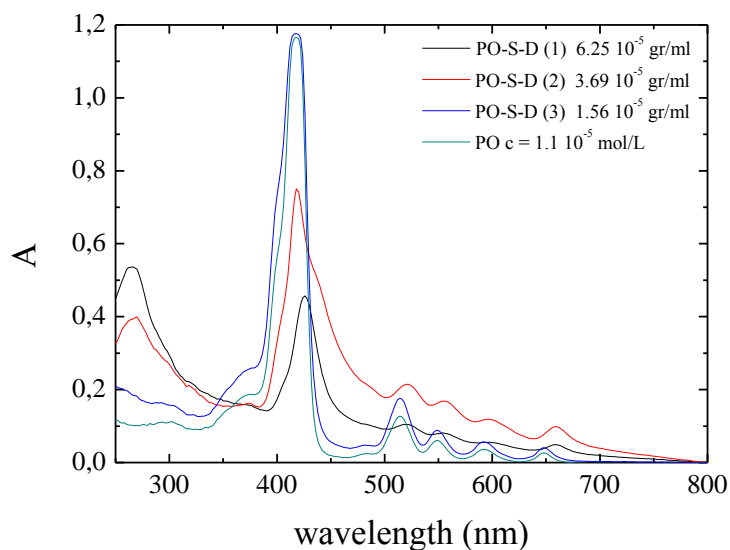


**Figure 3.16** UV/Vis spectra of samples PO-S-D (1), PO-S-D (2), PO-S-D (3) and PO at different particle concentrations.

**Table 3.4** Theoretical and experimental porphyrin content of the porphyrin-containing particles with 5 wt % AOT.

Sample	PO-St-DVB mole ratio	Theoretical porphyrin content (wt %)	Actual porphyrin content (wt %)
PO-S-D (1)	0.9-40-59.1	6.2	4.8
PO-S-D (2)	3.5-40-56.5	22.1	16.2
PO-S-D (3)	12-40-48	43.9	-

In the UV/Vis spectra of samples PO-S-D (1) and PO-S-D (2) a red-shift of the porphyrin peaks was observed which was attributed to possible PO-PO interactions. Thus, for better comparison between all samples the particle dispersions were all diluted to the same concentration of  $9.756 \cdot 10^{-6}$  gr/ml and then were measured again by UV/Vis (**Figure 3.17**).

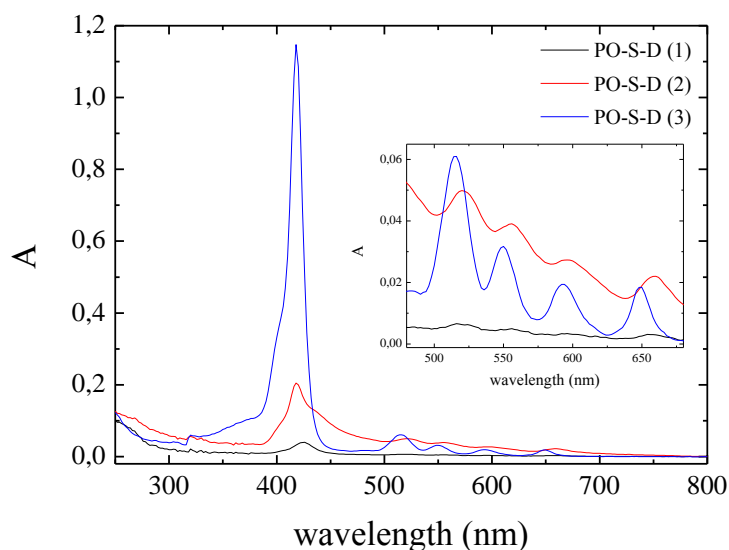


**Figure 3.17** UV/Vis spectra of samples PO-S-D (1), PO-S-D (2) and PO-S-D (3) at  $c = 9.756 \cdot 10^{-6}$  gr/ml. Inset: Higher magnification of the 480 to 680 nm range (Q-bands).

The same red-shift was again observed for samples PO-S-D (1) and PO-S-D (2). Since the red-shift was not eliminated by dilution of the samples it was attributed to porphyrin macrocycles within the particles forming intraparticle J-aggregates.<sup>[1]</sup>

### 3.4.4 Drying of the samples with supercritical point drying

After the synthesis of the samples the solvent-free open pores of the particles were obtained by supercritical point drying with CO<sub>2</sub>. The most commonly used solvent for this process is ethanol which however, is not a ‘good’ solvent for polystyrene, thus the particles were not expected to be swollen in ethanol. A second potential solvent used for supercritical point drying with CO<sub>2</sub> is DMF which is a better solvent for polystyrene and the porphyrin thus was used to swell the particle before the drying process.<sup>[2],[3]</sup>

First, the swelling of the particles in DMF was investigated by DLS. A single exponential decay of the autocorrelation functions and a linear increase of the decay rate with the square of the wavevector were found confirming the presence of a single

process (**Figure 3.18**). The diffusion coefficient of the single process for sample PO-S-D (1) was found to be  $D = 2.82 \cdot 10^{-12} \text{ m}^2/\text{s}$  which corresponds to a hydrodynamic radius of 83 nm (166 nm diameter). For sample PO-S-D (2) the diffusion coefficient of the single process was found to be  $D = 7.55 \cdot 10^{-13} \text{ m}^2/\text{s}$  which corresponds to a hydrodynamic radius of 309 nm (618 nm diameter). Finally, for sample PO-S-D (3) the diffusion coefficient of the single process was found to be  $D = 5.29 \cdot 10^{-13} \text{ m}^2/\text{s}$  which corresponds to a hydrodynamic radius of 441 nm (882 nm diameter).

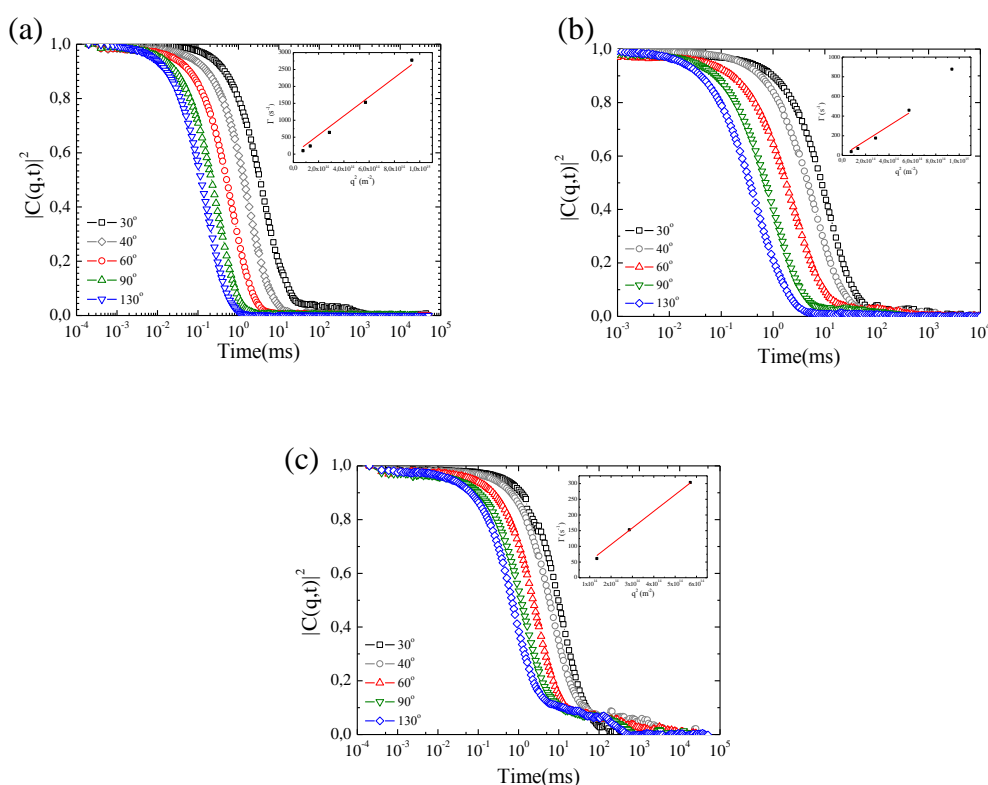


**Figure 3.18** Intensity autocorrelation function of the samples (a) PO-S-D (1), (b) PO-S-D (2) and PO-S-D (3) in DMF at different scattering angles. Inset: Decay rates of the autocorrelation functions ( $\Gamma$ ) as a function of the square of the wavevector ( $q^2$ ).

Based on these results it is clear that the particle size for all samples in DMF is larger compared to that found in water verifying the swelling of the particles in DMF which is a good solvent for the polymer. Moreover, the difference in the size between water and DMF increases as the porphyrin content of the particles increases (**Table 3.5**). Although these results at first seem to contradict the higher cross-link density of the samples as the porphyrin content of the particles increases, this is not the case,

since the effective cross-link density of the sample PO-S-D (3) is lower than PO-S-D (2) since it contains less DVB and PS. On the other hand, the lower degree of swelling of sample PO-S-D (1) in DMF despite its lower porphyrin content compared to the other two samples is possibly attributed to the absence of toluene during the synthesis of the particles. These swollen particles in DMF were then dried using supercritical point drying with CO<sub>2</sub> and were assessed as porous materials for gas separation of CO<sub>2</sub> from its mixture with CH<sub>4</sub>.

**Table 3.5** Hydrodynamic particle sizes in water and DMF for the porphyrin containing particles with 5 wt % AOT.

Sample	PO-St-DVB mole ratio	R <sub>h</sub> in water by DLS	R <sub>h</sub> in DMF by DLS
PO-S-D (1)	0.9-40-59.1	65 nm	83 nm
PO-S-D (2)	3.5-40-56.5	45 nm	309 nm
PO-S-D (3)	12-40-48	36 nm	441 nm

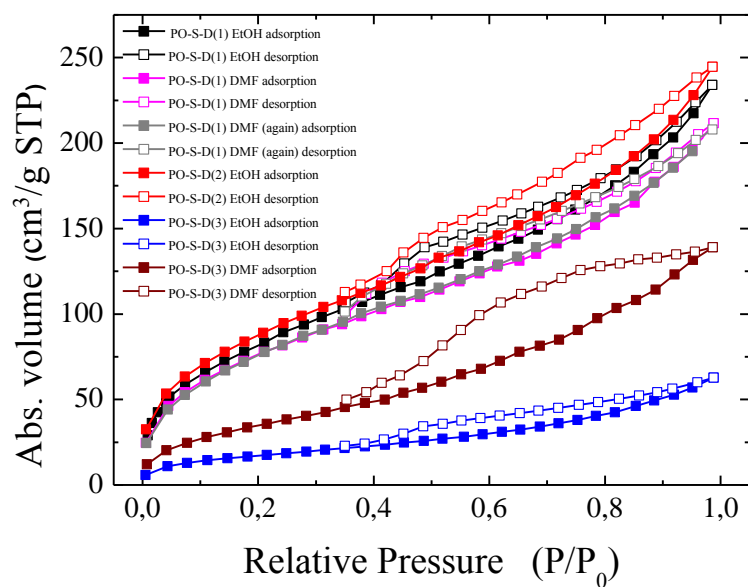
### 3.4.5 Surface area measurements of the porphyrin containing particles

Next, the porphyrin-containing particles were further investigated in order to examine their potential permanent porosity and surface area. The samples were exchanged from water to ethanol or DMF using a dialysis membrane with a MWCO limit of 3500 and then the solvent was removed with supercritical point drying using liquid CO<sub>2</sub>. Finally, the open pore structure of the polymer nanoparticles was obtained. Nitrogen and carbon dioxide adsorption/desorption measurements were used to determine the surface area and the porosity of the samples analyzing the results with the BET and the DR method.

### 3.4.5.1 Adsorption/desorption isotherms

The BET method was employed for the analysis of the nitrogen sorption measurements in order to determine the surface area of the samples, whereas the pore size distribution was calculated using the NLDFT method. All samples featured a typical IV type curve indicating the existence of both micro- and meso-pores. Sample PO-S-D (1) showed promising results when dried from EtOH reaching a surface area of  $317 \text{ m}^2 \text{ gr}^{-1}$ . However, despite these high expectations the surface area of PO-S-D (1) was similar when the sample was dried from DMF ( $291 \text{ m}^2/\text{gr}$ ) and even at longer drying times the surface area of the sample did not exceed  $299 \text{ m}^2 \text{ gr}^{-1}$  (**Figure 3.19 a**). These results lead us to the conclusion that the porphyrin content of PO-S-D (1) was low and thus the particles could not form an open pore structure in the solvent. Next, sample PO-S-D (2) was dried from EtOH using supercritical point drying with liquid  $\text{CO}_2$  and exhibited a BET surface area of  $334 \text{ m}^2 \text{ gr}^{-1}$ , which is only very slightly higher than that of PO-S-D (1). This increase was attributed to the higher porphyrin content of PO-S-D (2) compared to PO-S-D (1), however, the increase in the surface area was not very high because the particles were not swollen in ethanol during the drying process. It is also noted that both samples regardless of the solvent used for drying exhibited an average pore size of  $3.5 \text{ nm}$  (**Figure 3.19 b**). Finally, the sample PO-S-D (3) exhibited a completely different behavior compared to the two other samples, with a very low BET surface area of  $64 \text{ m}^2 \text{ gr}^{-1}$  and a pore size range from  $3.7$  to  $6.8 \text{ nm}$  when dried from EtOH. This was attributed to the use of a larger amount of toluene during the synthesis of the particles to solubilize the porphyrin, which potentially formed large voids inside the particles and led to a larger pore size and an overall lower surface area. This was also supported by the results obtained for PO-S-D (3) when dried from DMF which is a good solvent for polystyrene and porphyrin. In this case, the BET surface area was calculated  $136 \text{ m}^2 \text{ gr}^{-1}$ , which is almost twice higher than that found for the same sample when dried from EtOH, and this is due to the swelling of the particles in DMF, but is still much lower than that found for the other two samples and this is attributed to the presence of the large voids within the particles. The pore size of PO-S-D (3) when dried from DMF was found  $5.7 \text{ nm}$  suggesting again the presence of larger pores within these particles.

(a)



(b)

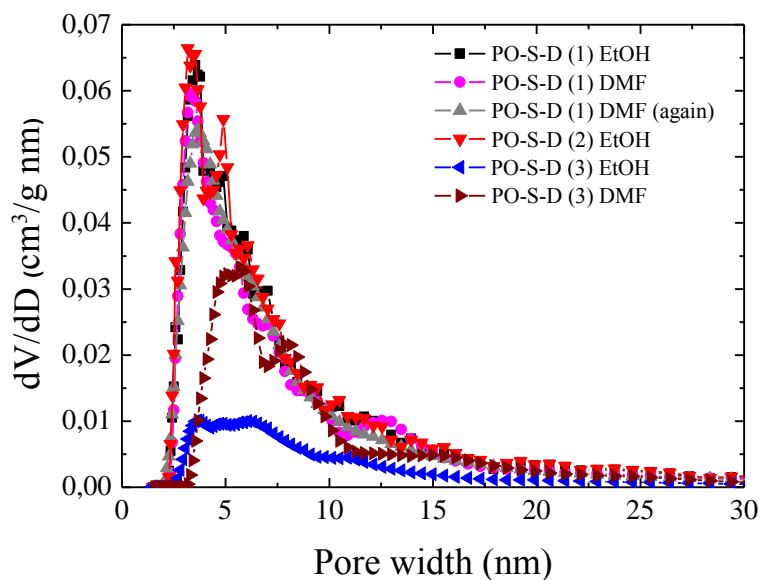
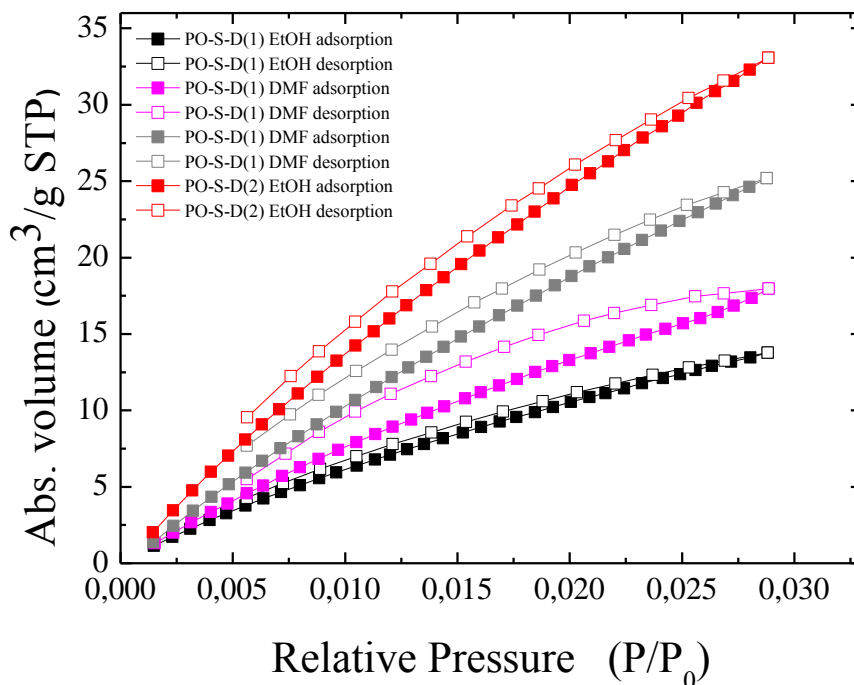


**Figure 3.19** (a) Nitrogen adsorption/desorption isotherms at 77K and (b) pore size distributions determined using the NLDFT method for PO-S-D (1) from EtOH (■) and DMF (■, ■), PO-S-D (2) from EtOH (■) and PO-S-D (3) from EtOH (■) and DMF (■).



In order to investigate the microporosity of the samples CO<sub>2</sub> adsorption/desorption isotherms were obtained and analyzed using the BET and the DR method. Sample PO-S-D (1) exhibited very poor results when dried from EtOH reaching a BET surface area of only 205 m<sup>2</sup> gr<sup>-1</sup>. Moreover, when dried from DMF sample PO-S-D (1) showed a BET surface area which was depended on the drying time. For shorter times (8 hours), the surface area was calculated 273 m<sup>2</sup> gr<sup>-1</sup> and increased to 501 m<sup>2</sup> gr<sup>-1</sup> when the sample was dried for ten hours, attributed to the longer interactions of liquid CO<sub>2</sub> with the surface of the sample leaving larger open pores when evaporated. On the other hand, sample PO-S-D (2) exhibited a remarkable BET surface area of 618 m<sup>2</sup> gr<sup>-1</sup> when died from EtOH, which was attributed to the higher PO content of the particles resulting in an open pore structure and to more micropores. It is also noted that both samples, regardless of the solvent used, exhibited a bimodal pore size distribution with maximum at 0.57 and 0.8 nm (**Figure 3.20**). Finally, sample PO-S-D (3) was not investigated due to the very poor results obtained for the nitrogen adsorption measurements.

(a)



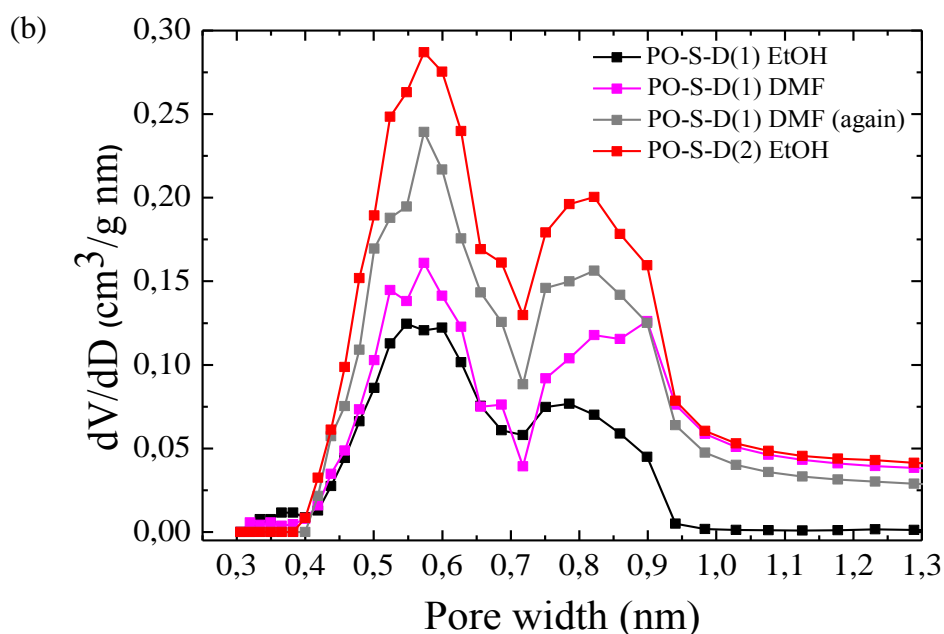


**Figure 3.20** (a) CO<sub>2</sub> adsorption/desorption isotherms at 0K and (b) pore size distributions determined using the NLDFT method for PO-S-D (1) from EtOH (■) and DMF (■, ■) and PO-S-D (2) from EtOH (■).

Further analysis of the CO<sub>2</sub> adsorption/desorption isotherms with the DR method gave the apparent DR surface areas which were in good agreement with the BET surface areas suggesting the intrinsic microporosity of these materials. More specifically, sample PO-S-D (1) reached a DR surface area of 214 m<sup>2</sup> gr<sup>-1</sup> when dried from EtOH, whereas, when dried from DMF the sample showed again a DR surface area which was depended on the drying time. Thus, for shorter drying times (8 hours) the DR surface area was calculated 283 m<sup>2</sup> gr<sup>-1</sup> and increased to 465 m<sup>2</sup> gr<sup>-1</sup> when the sample was dried for ten hours. On the other hand, sample PO-S-D (2) reached a DR surface area of 581 m<sup>2</sup> gr<sup>-1</sup> when dried from EtOH. The above results are summarized in **Table 3.6**.

**Table 3.6** Surface area, pore size and pore volume of the porphyrin containing particles dried from different dispersion media.

Sample	PO-St-DVB mole ratio	dispersion medium	surface area (m <sup>2</sup> /gr)			pore size (nm)		Total pore volume (cm <sup>3</sup> /gr)
			N <sub>2</sub> BET	CO <sub>2</sub> BET	CO <sub>2</sub> DR	N <sub>2</sub>	CO <sub>2</sub>	N <sub>2</sub> isotherm
PO-S-D (1)	0.9-40-59.1	EtOH	317	205	214	3.5	0.57 and 0.8	0.350
		DMF	291	273	283			0.314
		DMF*	299	501	465			0.310
PO-S-D (2)	3.5-40-56.5	EtOH	334	618	581			0.365
PO-S-D (3)	12-40-48	EtOH	64	-	-	3.7 - 6.8	-	0.094
		DMF	136			5.7		0.209

\*dried for longer time

Further analysis of sample PO-S-D (2) dried from DMF is in progress in order to verify the potential of this sample in gas separation applications.

### 3.4.6 Selectivity of CO<sub>2</sub> over CH<sub>4</sub>

The permanent microporosity and the high surface area of sample PO-S-D (2) suggested that it is a potential good candidate for investigating its ability to separate small molecules such as CO<sub>2</sub> and CH<sub>4</sub>. The analysis of the single-component isotherms using the IAST theory predicts the selectivity of the material for a CO<sub>2</sub>/CH<sub>4</sub> gas mixture. Sample PO-S-D (2) exhibited a remarkable separation performance with separation factors of 12 and 23 at 273 K and 263K, respectively, in the low pressure limit (**Figure 3.21 a**). The isosteric heat of adsorption ( $q_{st}$ ) was also determined for the probe molecules CO<sub>2</sub> and CH<sub>4</sub> by fitting the adsorption isotherms at 263 K and 273 K to the appropriate virial-type equations. For sample PO-S-D (2) the isosteric heat of adsorption was calculated ~24 and ~ 16 kJ mole<sup>-1</sup> for CO<sub>2</sub> and CH<sub>4</sub>, respectively at the limit of zero coverage (**Figure 3.22 b**).

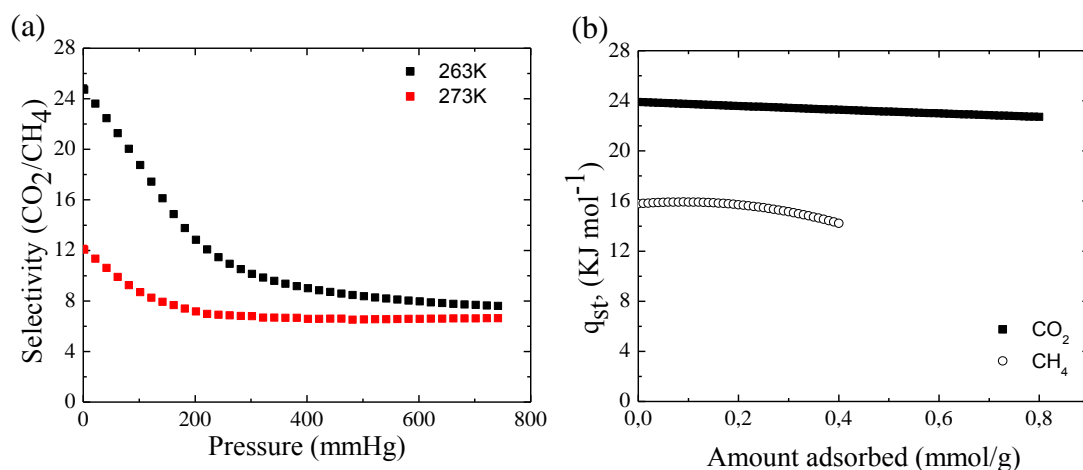


**Figure 3.22** (a) CO<sub>2</sub>/ CH<sub>4</sub> selectivity predicted by applying the IAST method to the CO<sub>2</sub> and CH<sub>4</sub> single-component isotherms at 263 (■) and 273 (■) K for the PO-S-D(2) sample; (b) Isosteric heat of adsorption for CO<sub>2</sub> (■) and CH<sub>4</sub> (○) as a function of adsorbed amount.

These results for CO<sub>2</sub>/CH<sub>4</sub> selectivity are exceptional compared to similar highly cross-linked polystyrene polymers synthesized without the porphyrin cross-linker which reached separation factors of ~7-13 and isosteric heat of adsorption values of ~22 and ~16 kJ mole<sup>-1</sup> for CO<sub>2</sub> and CH<sub>4</sub>, respectively at the limit of zero coverage.<sup>[4]</sup> Our results suggest that the presence of the porphyrin moieties within the polymeric network enhances the  $\pi$ -electron density of the material which interacts strongly with quadrupolar CO<sub>2</sub> but not with the nonpolar CH<sub>4</sub> molecules. This assumption is also supported by the high isosteric heat of adsorption values that indicate the presence of favorable adsorption interactions between the polar CO<sub>2</sub> and the highly electron-rich polymer surface area. Future studies for sample PO-S-D (2) dried from DMF are in progress and will further elucidate the behavior of this material in CO<sub>2</sub>/CH<sub>4</sub> separation by better accessing the open pore structure of the particles.

### 3.5 References

- [1] S. Deng and R.C. Advincula, *Macrom. Rapid Commun.* , 32 (2011) 1634.
- [2] Z. Wang, S. Yuan, A. Mason, B. Repogle, D.-J. Liu and L. Yu, *Macromolecules*, 45 (2012) 7413.
- [3] A. Fateeva, S. Devautour-Vinot, N. Heymans, T. Devic, J.-M. Grenèche, S. Wuttke, S. Miller, A. Lago, C. Serre, G. De Weireld, G. Maurin, A. Vimont and G. Férey, *Chem. Mater.*, 23 (2011) 4641.
- [4] M. Kaliva, G.S. Armatas and M. Vamvakaki, *Langmuir*, 28 (2012) 2690.

## 4 Conclusions

This master thesis reports the successful synthesis of microporous porphyrin containing polystyrene nanoparticles that are potential candidates for gas separation applications. Emulsion polymerization in water was used as a facile and versatile method to produce particles with sizes in the range of nanometers. The morphology and the size of the particles were investigated by SEM, TEM and DLS measurements. The PO content of the particles was determined by UV/Vis spectroscopy. Solid open-pore particles were obtained using supercritical point drying with liquid CO<sub>2</sub> to dry a dispersion of the particles in EtOH or DMF. The porosity and surface area of the particles were investigated by N<sub>2</sub> and CO<sub>2</sub> adsorption/desorption isotherms, analyzed using the BET and the DR method whereas, the NLDFT method was employed to determine the pore size distribution. Furthermore, the potential selectivity of the samples in CO<sub>2</sub>/CH<sub>4</sub> gas separation was calculated by analyzing the adsorption data using the ideal adsorption solution theory.

First, a series of polystyrene particles were synthesized in order to investigate the effect of the stabilizer, AOT, on the stability and size distribution of the particles. The successful synthesis of monodisperse PS particles was achieved using 1 wt % AOT. Next, a series of highly cross-linked PS colloidal particles were synthesized at a constant St:DVB mole ratio of 40:60 while altering the stabilizer content from 1 to 10 wt% with respect to the monomers. The increase in the stabilizer content led to a decrease of the size of the particles as expected. Moreover, the size of the highly cross-link PS particles was smaller compared to that of the PS particles without cross-linker at the same stabilizer content.

Based on the above results porphyrin-containing polystyrene particles were synthesized using 1 wt % AOT, however these particles were unstable and coagulated in the aqueous medium. In order to solve this problem we increased the stabilizer content from 1 to 5 wt % and prepared a series of porphyrin-containing colloidal particles at 5 wt % stabilizer with respect to the monomers while altering the PO content from 0.9 to 12 mole % based on the monomers content. The cross-link density of the particles increased significantly by increasing the tetra-functional porphyrin content whereas the size and size distribution of the particles decreased. Moreover, as

the PO content of the particles increased, a co-solvent (toluene) was necessary in order to solubilize the PO in the reaction medium. It was found that the addition of toluene caused the formation of large drops within the microgels which led to large voids and affected the morphology, the surface area and the porosity of the particles.

The dry open-pore samples were obtained using supercritical point drying with liquid CO<sub>2</sub> after dispersing the samples in either EtOH or DMF. Next, the N<sub>2</sub> adsorption isotherms were analyzed using the BET method. Samples PO-S-D (1) and PO-S-D (2) appeared to have similar BET surface area of about 300 m<sup>2</sup> gr<sup>-1</sup> and a pore size of 3.5 nm, when dried from EtOH and DMF. This result was attributed to the molecular kinetic diameter of nitrogen ( $d_k(\text{N}_2) \sim 3.6 \text{ \AA}$ ) and the temperature in which the experiment was conducted (77 K) which limited the diffusion of the gas molecules inside the particles structure. However, PO-S-D (3) showed a very low BET surface area of 64 m<sup>2</sup> gr<sup>-1</sup> when dried from ethanol, which was attributed to the presence of large voids inside the microgels causing the disruption of the network structure. On the other hand, PO-S-D (3) exhibited an increase in the surface area to 136 m<sup>2</sup> gr<sup>-1</sup> when dried from DMF, which is twice higher than the value found in ethanol but still much lower than the values found for PO-S-D (1) and PO-S-D (2) in either solvent.

The samples were further investigated by CO<sub>2</sub> adsorption/desorption isotherms and were analyzed using the BET and the DR methods. The results suggested that the surface area was dependent on the drying time and the PO content of the particles. When dried from EtOH, PO-S-D (1) exhibited an apparent BET and a DR surface area of 205 m<sup>2</sup> gr<sup>-1</sup> and 214 m<sup>2</sup> gr<sup>-1</sup>, respectively, whereas when dried from DMF the apparent BET surface area was 273 m<sup>2</sup> gr<sup>-1</sup> for shorter drying times and increased 501 m<sup>2</sup> gr<sup>-1</sup> for longer drying times. The DR method showed a similar behavior with a surface area of 283 m<sup>2</sup> gr<sup>-1</sup> for shorter trying times and 465 m<sup>2</sup> gr<sup>-1</sup> for the longer drying times. These results can be attributed to the absorption of liquid CO<sub>2</sub> within the material during the drying process causing the pores of the particles to remain open when CO<sub>2</sub> was evaporated. PO-S-D (2) exhibited the most promising behavior with an apparent BET surface area of 618 m<sup>2</sup> gr<sup>-1</sup> and a DR surface area of 581 m<sup>2</sup> gr<sup>-1</sup> when dried from EtOH. This was attributed to the increase in the PO content of the particles from 0.9 to 3.5 mole % which led to the formation of more pores (an increase in the pore volume was also observed), thus increasing the interactions of CO<sub>2</sub> with more exposed active sites inside the particle (porphyrin macrocycle and

phenyl groups of St and DVB). Moreover, the good agreement between the apparent BET surface areas and the DR surface areas led to the assumption that the samples are mainly microporous.

Finally, PO-S-D (2) which exhibited the most promising behavior was further investigated for separation of CO<sub>2</sub> and CH<sub>4</sub> by analyzing the single-component adsorption data using the ideal adsorption solution theory. Sample PO-S-D (2) exhibited a remarkable separation performance compared to previously synthesized PS particles, with separation factors of 12 and 23 at 263 K and 273K, respectively, in the low pressure limit. The isosteric heat of adsorption ( $q_{st}$ ) was also determined for the probe molecules, CO<sub>2</sub> and CH<sub>4</sub>, and was found ~24 and ~ 16 kJ mole<sup>-1</sup> for CO<sub>2</sub> and CH<sub>4</sub>, respectively at the limit of zero coverage. These results suggest that the porphyrin-containing colloidal particles are potentially attractive candidates for gas capture and the selective carbon dioxide separation from methane, although further studies of the selectivity of PO-S-D (1) and PO-S-D (2) when dried from DMF are required.



## 5 Characterization Techniques

### 5.1 Scanning Electron Microscopy (SEM)

The scanning electron microscope is designed to provide high-resolution, high-magnification images of a sample placed on a surface, even though it operates at low electron beam currents. A tungsten filament emits electrons, which are focused by an electron optical system. The electron beam can scan the sample surface and can provide composition at a point, along a line or over a rectangular area, by scanning the beam across the surface in a series of parallel lines. The sample is mounted on a stage that can be accurately moved in all three directions (x, y and z), normal to the plane of the sample. SEM can produce magnified images from virtually any type of specimen. The instrument generally operates in a high vacuum and a very dry environment in order to produce the high energy beam of electrons needed for imaging. Thus, most specimens destined for study in the SEM are poor conductors, with a few notable exceptions. In the SEM, the imaging system depends on the specimen being sufficiently electrically conductive to ensure that the bulk of the incoming electrons go to ground. The formation of the image depends on collecting the different signals that are scattered as a consequence of the high electron beam interacting with the sample. The two principal signals used to form images are backscattered electrons and secondary electrons generated within the primary beam-sample interactive volume. The backscattered electron coefficient increases with increasing atomic number of the specimen, whereas the secondary electron coefficient is relatively insensitive to atomic number. This fundamental difference in the two signals has an important effect on the way samples may need to be prepared. The use of scanning electron microscopy may be considered when being able to interpret the information obtained from the SEM and attempt to relate the form and structure of the two-dimensional images and identity, validity and location of the chemical data back to the three-dimensional sample from which the information was derived. A schematic representation of a SEM setup is depicted in **Figure 5.1**.

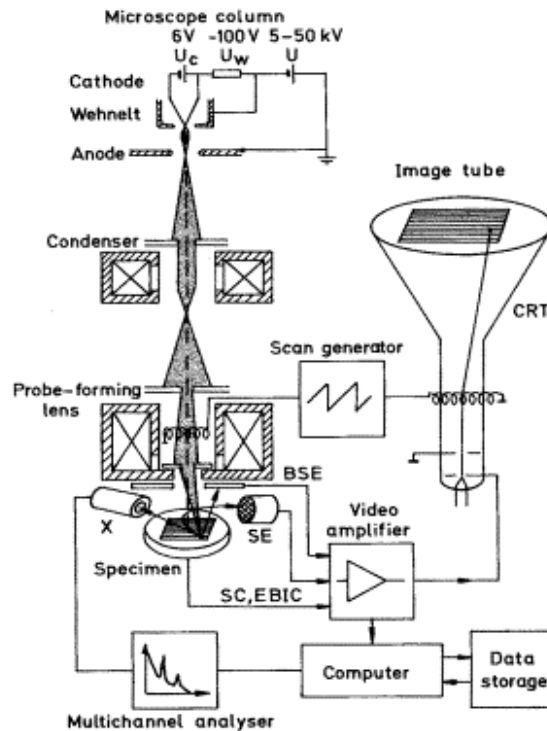


**Figure 5.1:** Schematic representation of a typical SEM setup.

## 5.2 Transmission Electron Microscopy (TEM)

Transmission electron microscopy (TEM) is a very powerful and useful technique for imaging materials in material science. This experimental technique is used for observing features such as the crystal structure, the growth of the layers, and the size of nanostructures and can be also used for the chemical analysis of the samples. TEM is based on the same basic principles as the light microscopes but instead uses electrons, and since their wavelength is smaller the resolution of the TEM images is higher. These highly energetic electrons interact with the atoms in the sample and produce characteristic radiation that is used in material characterization.

The microscope consists of the electron source, the electromagnetic lenses, the specimen area and the viewing screen. The electrons are usually generated by passing an electric current through a tungsten filament at the top of the column. The electrons are accelerated using high voltage in the range of 80 to 200 kV. This voltage accelerates the electrons down the column, towards the specimen. The beam of electrons strikes the specimen using condenser lens. Parts of the electrons are transmitted and focused by the objective lens forming an image at the viewing screen.

The images appear to have darker and lighter areas corresponding to less and more electrons transmitted through, respectively (**Figure 5.2**). The most important part is the sample preparation since the specimen must be thin enough in order to transmit enough electrons to form the image without using too much energy. Polymers are usually diluted enough and placed on the grid in order to dry. Since polymers are soft materials the voltage used to accelerate the electrons is usually ~ 80 kV.

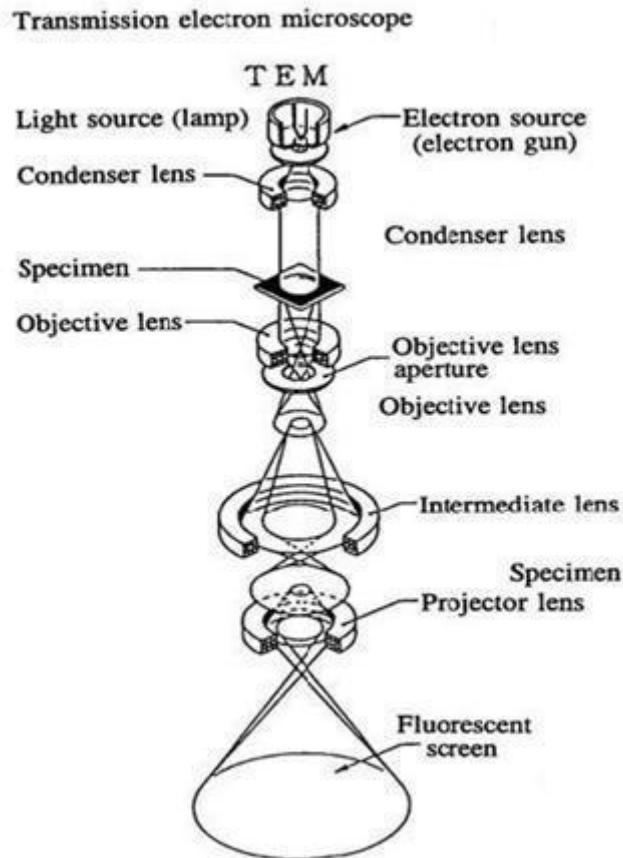


**Figure 5.2** Schematic representation of a typical TEM setup describing the path of the electron beam.

### 5.3 Dynamic light scattering (DLS)

Light scattering is a powerful tool for the characterization of the size and the shape of polymer nanoparticles in a solution. The monochromatic, coherent laser beam hits the particles, which is scattered and due to the Brownian motion of the particles that changes their distance in the solution a time-dependent fluctuation of the scattering intensity is observed. Changing the observation angle ( $\theta$ ) and thus the scattering vector ( $q$ ) a measure of the size is provided. The form factor that is the interference pattern of the scattered light is characteristic of the size and shape of the scatterer. The larger the particle is the slower the Brownian motion. Accuracy and stability of the temperature during the entire measurement is essential since the viscosity of the liquid is related to the temperature [Figure 5.3].

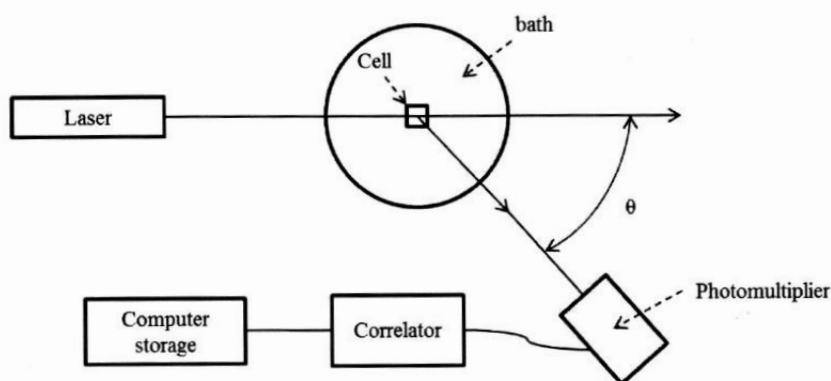


**Figure 5.3** Schematic representation of the experimental setup of the dynamic light scattering technique.

The velocity of the Brownian motion is defined by the translational diffusion coefficient ( $D$ ). The Stocks-Einstein equation is used in order to calculate the particles size based on the translational diffusion coefficient,

$$R_h = \frac{k_B T}{6\eta\pi D}$$

$R_h$  =hydrodynamic radius

$\eta$  =viscosity of the solvent

$k_B$  =Boltzmann constant

$T$  =temperature of the sample

The hydrodynamic radius refers to how the particle diffuses within the liquid solvent and is the same as that of a hard sphere with the same translational diffusion coefficient ( $D$ ) as the particle. The translational diffusion coefficient depends on various factors such as the size of the particle, the surface structure, the concentration of the sample and the type of ions in the medium. As depicted in **Figure 5.4** for a system of particles under constant, random Brownian motion a speckle pattern is observed. The phase addition from the moving particles is constantly evolving and forming new patterns. These intensity fluctuations of the scattered light are depending on the size of the particles and the time. Small particles cause the intensity to fluctuate more rapidly than larger ones.

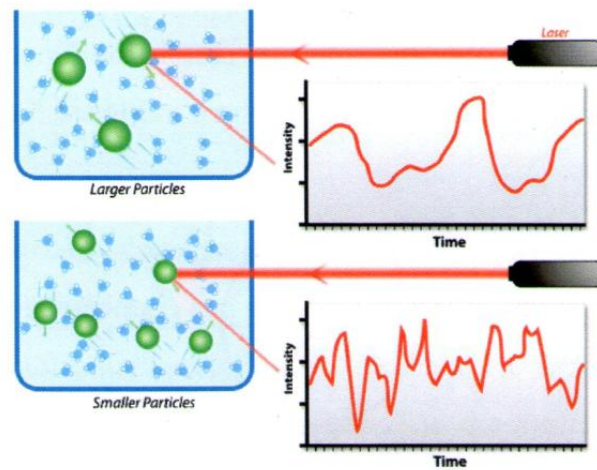


**Figure 5.4** Schematic illustrations of the intensity fluctuations of larger and smaller particles.

For a large number of monodisperse particles in Brownian motion, the correlation function  $G$  is an exponential decaying function of the correlator time delay  $\tau$

$$G(\tau) = A [1 + B \exp(-2\Gamma\tau)]$$

$A$  = baseline of the correlation function

$B$  = intercept of the correlation function

and  $\Gamma$  is given by the equation  $\Gamma = Dq^2$  where  $D$  is the translational diffusion coefficient and the wavevector  $q$  is given by

$$q = \frac{4\pi n}{\lambda} \sin\left(\frac{\theta}{2}\right)$$

$n$  = refractive index of the dispersant

$\lambda$  = wavelength of the laser

$\theta$  = scattering angle

## 5.4 Ultraviolet/visible spectroscopy (UV/Vis)

UV/Vis spectroscopy is a frequently used technique for the characterization of polymers and the investigation of additives in polymers. The range of wavelengths that correspond to the UV/Vis spectrum is from 200 to 800 nm, from which 200-400 nm is the ultraviolet region and 400-800 nm is the visible region. The energy that corresponds to these wavelengths is of the same magnitude as the energy difference between the electronic states of molecules. Thus when UV/Vis light strikes the sample the molecules absorb this energy and electronic transitions occur. The absorbance  $A$  can be defined by the Beer-Lambert-Bouguer law that correlates the absorption with the concentration of the absorbing species as shown in the following equation:

$$A = \epsilon bc$$

where  $\epsilon$  is the absorption coefficient (which is constant for a specific substance but depends on the wavelength, the solvent and the temperature),  $b$  is the thickness of the cuvette and  $c$  is the concentration of the sample.

For the correct application of the Beer-Lambert-Bouguer law five conditions should enforce:

1. The incident radiation should be monochromatic.
2. All rays of the incident radiation should travel parallel through the absorbing sample.
3. The incident radiation should not be sufficient to significantly alter the ground-state population of the absorbing molecules.
4. The absorbing sample must be homogeneous and scattering or reflection of the incident radiation should not occur.
5. The absorbing sample must be dilute enough so that no molecular interactions take place between the molecules.

## 5.5 $^1\text{H}$ NMR spectroscopy

NMR spectroscopy is a very useful and common technique for the structural characterization of chemical compounds.  $^1\text{H}$  NMR and  $^{13}\text{C}$  NMR are the more commonly used for the characterization of materials. NMR spectroscopy is based on the principal of nuclei being positively charged spinning on an axis and forming a tiny magnetic field. This nuclear magnetic field can either align or oppose with an external magnetic field  $B_0$  (**Figure 5.5**).

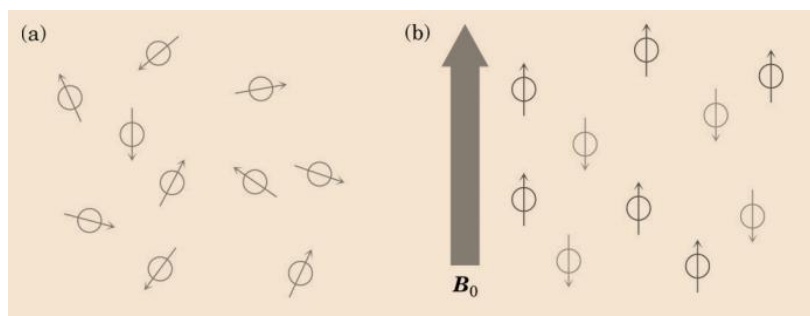


**Figure 5.5** (a) Random orientation of the nuclear magnetic fields in the absence of an external magnetic field ( $B_0$ ), (b) Aligned or opposed nuclear magnet fields in the presence of an external magnetic field ( $B_0$ ).

Different nuclei absorb electromagnetic irradiation at different wavelength depending on the chemical and electronic environment. The position and the pattern of the NMR signal provide the required information regarding the environment of the nuclei. The exact field strength (in ppm) of a nucleus comes into resonance relative to a reference standard, usually the signal of the deuterated solvent used. Electron clouds “shield” the nuclei from the external magnetic field causing them to absorb at higher energy (lower ppm) whereas the neighboring functional groups “deshield” the nuclei causing them to absorb at lower energy (higher ppm). Chemically and magnetically equivalent nuclei resonate at the same energy and give a single signal or pattern. Protons on adjacent carbons interact and “split” each other’s resonances into multiple peaks following the  $n + 1$  rule with a coupling constant  $J$ . Spin-spin coupling is commonly observed between nuclei that are one, two and three bonds apart. The area under an NMR resonance is proportional to the number of nuclei that give rise to that resonance, thus by integration the protons of that resonance can be calculated.